UNIVERSITY OF COPENHAGEN

Master of Science in Physics

Understanding Black Hole Spectroscopy

Lucía Vélez Tartajo

Supervised by Vítor Cardoso

May 2026

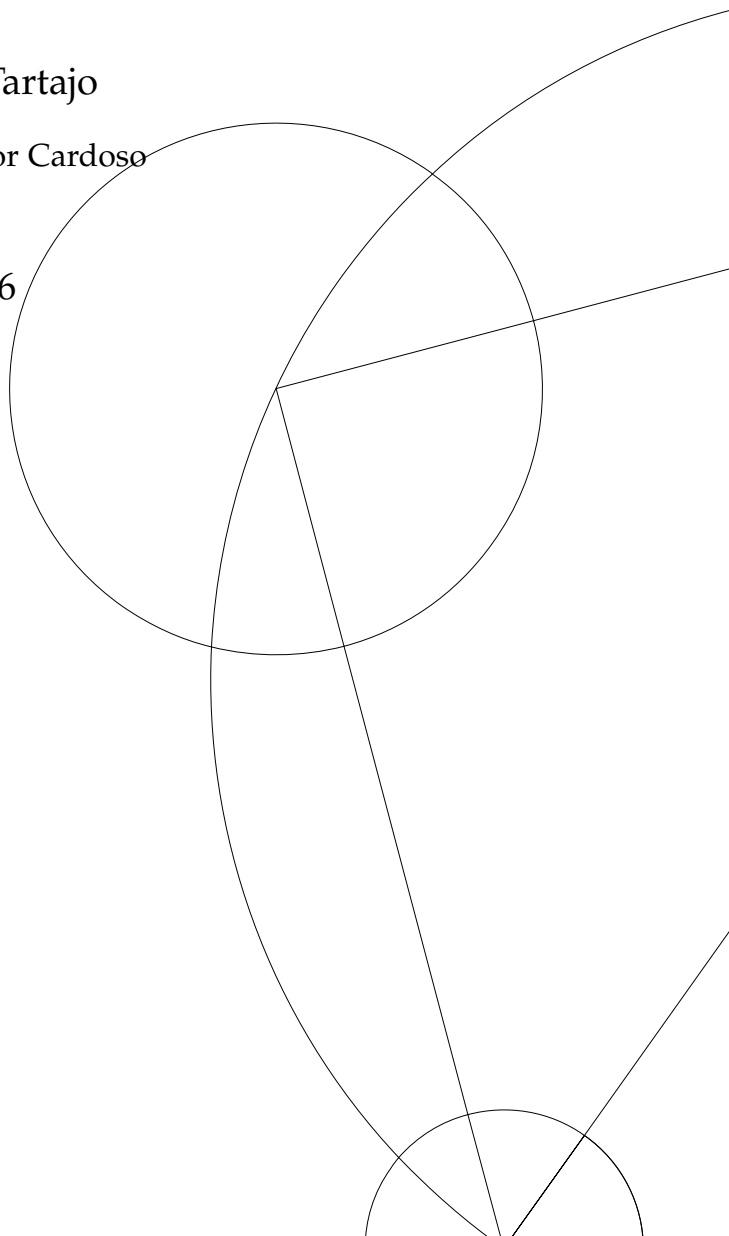

Lucía Vélez Tartajo

Understanding Black Hole Spectroscopy

MSc in Physics, May 2026

Supervisor: Vítor Cardoso

University of Copenhagen

Faculty of Science

Niels Bohr Institute

Blegdamsvej 17

Copenhagen N

A mis padres, Paqui y Luis.

ACKNOWLEDGEMENTS

First and foremost, I want to express my deepest gratitude to my supervisor Vítor Cardoso. When I was applying to MSc programmes across Europe, it was always my dream to come to Copenhagen and, hopefully, work in some project with you. Writing my thesis under your supervision has been a privilege for which I will remain forever grateful. I sincerely thank you for pushing me to always give my best, for teaching me thought your example what it means to be a great researcher, and for your patience and confidence in me throughout this journey.

I am also deeply indebted to Jaime Redondo, my unofficial co-supervisor. I will always be grateful for your kindness and openness, from the very first time we met at the beginning of my master's, when you encouraged me to come to a Strong group meeting. I don't think I would be here today had it not been for that small but decisive act. Working with you over these months has been a true pleasure and has taught me how to ask the right questions, not be afraid of seeking answers, and to have confidence in myself.

Moreover, I want to thank Maarten van de Meent. It has been a pleasure working with you in my first real research project, and I am truly grateful that you agreed to continue the project beyond my PUK. Through this process, I have learnt a great deal about GR, Mathematica, and using the cluster, skills that will undoubtedly prove invaluable in my future career.

I also need to thank my partner in crime, Leart Sabani. Through endless discussions over coffee and walks in the park, I have learnt not only about physics and black holes, but also what it means to be a good friend. Sharing this experience with you has made it significantly more bearable, especially in those moments when neither of our codes wanted to work and we would fall into despair together. Tak for i år.

I also want to thank every member of the Strong group for all the discussions, hangouts, and fun we moments of joy we have shared over these almost two years. I am proud have been part of this group of extraordinary human beings that not only do remarkable physics, but also have immense hearts. Special thanks to Lorena for always being there; to Guangzi for welcoming us into the PhD office of the third floor; to Conor and Luka for the fun nights; and to David, Jaime, and Jann for the climbing sessions.

Thank you to my friends, both in Madrid and in Copenhagen. Special thanks to Rubén for endless conversations about the deepest topics and for always making me laugh, even in the

toughest moments; to Lena for the countless climbing (and yapping) sessions and girls' nights; and to Miguel and Ceballos for the continued support from afar.

Finalmente, quiero dar las gracias a mi familia por su apoyo incondicional. A mi hermana de corazón, Laura, por siempre estar ahí, por inspirarme, apoyarme y creer en mí. Por sacarme a la montaña cuando la vida se vuelve demasiado ruidosa, por destrozarme jugando al tenis y por hacerme sentir como en casa cada vez que estoy contigo. A mi persona favorita, Jorge, por creer en mí más de lo que yo misma he sabido hacer. Tu apoyo y fe en mí son un faro que me guía en los momentos más oscuros. Gracias por inspirarme a ser mejor persona cada día, y por hacerme de rabiar cuando me ofusco. En estos dos años de incontables videollamadas y vuelos hemos estado separados por más de 700 km, pero te he sentido más cerca que nunca. Por último, pero no menos importante, a mis padres, Paqui y Luis. Gracias por haber confiado en mí y por haberme dado alas para volar y conocer mundo. Gracias por haberme enseñado a trabjar duro y a luchar por mis sueños. Gracias por vuestro amor y vuestro apoyo constante.

ABSTRACT

Black hole spectroscopy is a vibrant field of research that uses the quasinormal mode spectrum to infer properties of black hole spacetimes, providing a powerful probe of gravity in the strong field regime, where deviations from general relativity may become observable. Despite its importance and significant development in recent years, the mechanism by which quasinormal modes are excited remains elusive and poorly understood, particularly in relation to light ring physics. In this thesis, we investigate how the properties of a perturbation determine the amplitude of the excited quasinormal modes, and whether the excitation process can be regarded as localized in spacetime, thus quantifying how the properties of the perturbations translate to quasinormal mode excitation. To address these questions, we analyse a series of simplified scenarios on a non-rotating background that serve as controlled probes of mode excitation.

We first consider the homogeneous perturbation equation and study how quasinormal mode excitation depends on the different parameters characterizing the initial conditions, which we take to be Gaussian. We find that wider initial data suppress quasinormal mode excitation, suggesting that adiabatic perturbations enhance the late-time tail over ringdown. We also examine the dependence on the location of the initial perturbation and find that overtone amplitudes are strongly suppressed relative to the fundamental mode when the initial perturbation is placed in the neighbourhood of the light ring. This result indicates that the observation of overtones in a ringdown signal cannot arise from perturbations confined exclusively to the light ring region.

We then study the source-driven problem, considering a scalar perturbation sourced by a radially infalling point particle with tunable velocity. Depending on the velocity of the particle, two distinct ringdown windows can be observed: the first one associated with the scattered radiation sourced by the motion of the particle and the second triggered by the particle itself crossing the light ring, each with a different mode content. Finally, we study the effect of the source on the signals. We find that switching off the source after it crosses the peak of the potential barrier produces only minor changes in the signal, indicating that the radiation generated inside the light ring region contributes negligibly to observers at infinity; this also has practical implications for computationally expensive simulations.

CONTENTS

1

INTRODUCTION

From the earliest attempts to understand and quantify the motion of stars to the modern detection of gravitational (GWs), our understanding of the universe has always been driven by a persistent curiosity about phenomena that lie beyond direct experience. In this pursuit, theoretical constructs are only as meaningful as the signatures they imprint on observable quantities. Black holes (BHs), once regarded as only mathematical curiosities of General Relativity and lying far away from reality, have now entered the realm of observation through their dynamical interactions and in particular the radiation they emit. These signals serve as probes of the underlying spacetime geometry and of the theoretical framework from which they arise.

Throughout history, the nature of gravity has undergone a conceptual evolution, reflecting increasingly refined attempts to describe motion in the universe. Early philosophers, such as Aristotle, interpreted motion as a consequence of the object's intrinsic nature, with no notion of gravity as a universal interaction. This conception was gradually replaced during the scientific revolution, most notably through the work of Galileo Galilei, who established both a mathematical and experimental framework for the study of motion, revealing that bodies fall in the same way independently of their mass.

A change of paradigm occurred in the 17th century with Isaac Newton and the publication of *Philosophiæ Naturalis Principia Mathematica* [1], in which he presented his three laws of motion as well his law of universal gravitation. In this description, gravity is formulated as a universal force acting between masses according to a precise mathematical law. Despite its remarkable success, Newtonian gravity ultimately proved incomplete, as evidenced by phenomena such as the anomalous precession of Mercury's orbit. This limitation was resolved in 1915, when Albert Einstein introduced the *General Theory of Relativity* (GR) [2], revolutionizing our understanding of gravity. GR is a geometric, non-linear theory, in which gravity is interpreted as a manifestation of the spacetime curvature rather than as a force. In this framework, spacetime itself becomes a dynamical entity, whose geometry is determined by

the distribution of matter and energy through the Einstein field equations. These equations establish a direct relation between the curvature of spacetime and its matter and energy content, encoded into the energy-momentum tensor. This interplay is perfectly captured by the famous quote by John Archibald Wheeler: "*Spacetime tells matter how to move; matter tells spacetime how to curve.*" [3] The motion of bodies then follows from this curvature. One of the most striking predictions of this theory is the existence of BHs, extreme manifestations of gravity. BHs are regions of spacetime in which the curvature becomes so extreme that it fundamentally alters the causal structure of spacetime, to the extent that not even light can escape from them.

Despite the complexity of the theory from which they arise, BHs are remarkably simple, since their properties are fully determined by only three parameters: the mass, spin, and charge. This simplicity is formalized by the no-hair theorem, which states that all stationary, asymptotically flat BH solutions to the four-dimensional Einstein-Maxwell equations are completely characterized by these three quantities [4–9]. In this context, all such solutions can be viewed as belonging to a single three-parameter family, whose most general member is the Kerr-Newman geometry, which describes the most general and asymptotically flat BH with both spin and charge [10]. The remaining solutions can be seen as arising from particular limits of this geometry. Historically, however, these solutions were derived in a more incremental way. The Schwarzschild solution, which is the only spherically symmetric solution to the vacuum Einstein equations, describes a non-rotating, uncharged BH [11], and corresponds to the vanishing spin and charge limit. The Kerr solution generalizes this result to include rotation [12], and is recovered from the Kerr-Newman family by setting the charge to zero. The Reissner-Nördstrom solution, which is the only spherically symmetric and asymptotically flat solution of the Einstein-Maxwell equations, accounts for electric charge [13, 14], and corresponds to the vanishing spin limit. The Kerr–Newman solution was the last one obtained, completing the family as the most general stationary BH solution in the Einstein-Maxwell theory. Astrophysical BHs, however, are expected to be effectively neutral, since any significant charge would rapidly attract surrounding plasma and opposite charges from the environment, leading to efficient neutralization. As a result, charge is not generally expected to play an important role in realistic astrophysical scenarios, and rotating BHs are typically described by the Kerr geometry.

In GR, GWs are generated by a wide variety of dynamical processes involving non-spherically symmetric mass-energy configurations, as they are sourced at leading order by time-variations of the system's quadurpole moment [15, 16]. Astrophysical sources include compact binary coalescences of neutron stars and BHs [17, 18], core-collapse supernovae [19], rapidly rotating

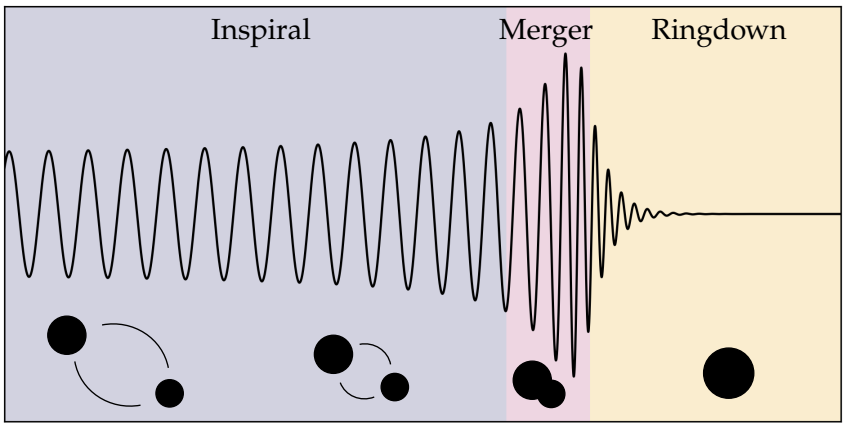

Figure 1.1: Illustration of the inspiral, merger, and ringdown phases in the evolution of a compact binary.

neutron stars [20], and, potentially, stochastic backgrounds of cosmological origin, e.g. from phase transitions [21]. Within this broader context, dynamical processes involving BHs, such as binary inspirals and mergers, constitute some of the most powerful and clean sources, generating disturbances in the spacetime geometry that propagate through the cosmos as gravitational radiation. Mathematically, GWs arise from considering perturbations on a given spacetime, and they provide an essential tool to study the dynamics of spacetime. Although this phenomenon was predicted as a direct consequence of GR, their direct detection remained elusive for nearly a century, until September 2015, when the first detection finally took place by the LIGO and Virgo collaborations [18, 22]. Since then, hundreds of such events have been observed, providing a wealth of information about BHs and their properties through the analysis of the detected waveforms. We have learned that GWs propagate at the speed of light [23], that intermediate-mass BHs exist and can form through GW-driven mergers [24], and that GR remains remarkably accurate in the strong-field and highly dynamical regime [25–28]. Looking ahead, the next generation of gravitational wave detectors, including the Laser Interferometer Space Antenna (LISA) [29], Einstein Telescope (ET) [30], and Cosmic Explorer (CE) [31], is expected to significantly enhance the sensitivity and frequency coverage of such observations. These instruments will enable the detection of a much larger number of events with higher signal-to-noise ratios, opening the door to a new era of precision GW astronomy.

The coalescence process of two BHs can be roughly divided into three stages, according to their orbital separation, as illustrated in Figure 1.1. In the initial inspiral phase, the BHs orbit each other while emitting energy in the form of GWs, gradually decreasing their separation. As they approach one another, they eventually become sufficiently close to form a common horizon, marking the onset of the merger phase. Following the merger, the newly formed BH undergoes a transient phase of damped oscillations as it settles into equilibrium, in close

analogy with the ringing of a struck bell. This stage, known as the ringdown, is the focus of BH spectroscopy [32, 33]. This portion of the GW has now been directly observed in high signal-to-noise events, most notably GW250114, one of the loudest GW detections to date [25, 34]. By analysing the information encoded in this phase, it is possible to infer properties of the remnant BH, such as its mass and spin, and to test GR in a regime that is otherwise inaccessible. As detector sensitivities continue to improve, ringdown signals are becoming increasingly relevant for both parameter estimation and fundamental physics [35–37]. Moreover, with the next generation of GW detectors it will be possible to probe the ringdown phase in greater detail, allowing to test the predictions of GR with unprecedented precision in the strong-field regime [38, 39].

BH spectroscopy has emerged as one of the most active and rapidly developing areas within gravitational physics in recent years. From a theoretical standpoint, the ringdown phase can be described with remarkable accuracy using linear BH perturbation theory, in which the signal is modelled as a superposition of exponentially damped sinusoids known as quasinormal modes (QNMs) [32, 33, 40–43]. These modes are characterized by complex frequencies that depend solely on the BH parameters. Conceptually, this description is analogous to the sound produced by a vibrating string: the resulting motion can be decomposed into a set of characteristic tones, or modes, each with a well-defined frequency [43]. In the case of BHs, there exists, in principle, an infinite tower of such modes. The longest-lived contribution, which typically dominates the signal, is referred to as the fundamental mode, while the more rapidly decaying contributions are known as overtones, resembling music. The QNM spectrum has been computed with remarkable precision over the past decades [42], with ongoing efforts aimed at achieving even higher accuracy. It has also been determined with high precision in a variety of beyond-GR theories [33]. In the absence of fully generic inspiral-merger-ringdown models in such frameworks, QNMs currently provide one of the most powerful probes of deviations from GR. However, despite this progress, significantly less is understood about the mechanisms by which these modes are excited in realistic dynamical scenarios. In particular, the determination of their amplitudes and relative excitation remains a central open problem in BH spectroscopy [44–49]. Addressing this issue is crucial for the interpretation of observed signals, for the construction of accurate and reliable waveform models, and ultimately for robust tests of GR [50].

This thesis aims to contribute to the understanding of the mechanisms governing the excitation of QNMs and its dependence on the properties of the perturbation. In particular, we address three central questions: under what conditions QNMs are excited, which features

of the perturbation control their amplitudes, and to what extent the process can be regarded as localized in spacetime. To this end, we analyse a series of simplified setups that serve as controlled probes of excitation. First, we investigate the dependence of QNM excitation on the choice of initial data for the perturbation equations. We then extend this analysis by introducing an explicit source, examining how this term modifies the excitation mechanism and gives rise to new features. Although the scenarios considered are intentionally idealized and simplified, they isolate the key ingredients of the problem and provide intuition that can be carried over to more realistic dynamical scenarios.

OUTLINE OF THE THESIS The thesis is organised as follows. We introduce the theoretical framework needed for our work in Section 2. We begin by reviewing the basic concepts of BH perturbation theory, and we derive the equation ruling gravitational perturbations on a Schwarzschild background. We also explain the approximation of the ringdown signal as a sum of QNMs, and their relation to light ring physics. In Section 3 we present the numerical methods used to solve the perturbation equations, and the convergence test performed to test the robustness of our algorithm. Moreover we introduce the Matrix Pencil Method, which we use to extract the QNM amplitudes from fits to the numerical solutions. Next, in Section 4, we consider the homogeneous perturbation equation and study the structure of the numerical solutions. We also study the mode content of such signals. In particular, we investigate how the mode excitation depends on the fitting window chosen to extract the amplitudes, as well as how it changes when varying the parameters characterizing the initial data we use to solve the perturbation equation. In Section 5 we consider the excitation produced by a radially infalling particle. Rather than solving the full gravitational perturbation problem, we adopt a simplified model in which a scalar field is sourced by a point-particle moving along a non-geodesic trajectory. We analyse the resulting numerical solutions and their dependence on the particle's velocity, and we investigate how the presence of the source influences both the signal and its QNM content. Finally, in Section 6, we summarise our main results and their implications, concluding with a brief outlook on possible future directions.

NOTATION AND CONVENTIONS. Throughout this thesis, we use the metric signature $(-,+,+,+)$ and geometrized units, $c = G = 1$. We denothe the covariant derivative associated with the metric by ∇, and the partial derivative by $\partial_\mu = \partial/\partial x^\mu$. We use Greek letters $\mu, \nu, ... = 0, 1, 2, 3$ to denote spacetime indices. We use the shorthand $\sum_{\ell m} \equiv \sum_{\ell=0}^{\infty} \sum_{m=-\ell}^{\ell}$ when summing over harmonics.

2

FRAMEWORK

In this section, we introduce the theoretical framework underlying this thesis. We begin with a review of the foundations of BH perturbation theory in Section 2.1. We then present the description of the ringdown phase and its characterization in terms of QNMs in Section 2.2. Finally, we explore the connection between the QNMs and the properties of the light ring in Section 2.3.

2.1 BLACK HOLE PERTURBATION THEORY

BH perturbation theory is the framework used to study how a BH spacetime reacts to a small disturbance. Instead of solving the Einstein equations exactly, BH perturbation theory treats the deviations from a known BH solution as small perturbations and analyses their evolution. This framework emerged in the late 1950s from efforts to assess BH stability. Regge and Wheeler (1957) analysed perturbations of the Schwarzschild metric, introducing an odd-parity decomposition and a Schrödinger-like master equation, recasting the problem as linear wave scattering [51]. Zerilli (1970) completed the treatment with even-parity modes [52], while Vishveshwara identified QNMs, establishing BHs as resonant systems [53]. The extension to rotating BHs was achieved by Teukolsky, whose master equation unifies the treatment of scalar, electromagnetic, and gravitational perturbations [54]. Subsequent refinements by Detweiler (QNM spectra, radiation reaction) and the synthesis by Chandrasekhar (axial-polar relations and symmetries) consolidated the formalism [40, 55].

We now study linear perturbations of the Schwarzschild metric and derive the equation governing their dynamics. Let us begin by considering a perturbation on a Schwarzschild background,

$$g_{\mu\nu}(x) = \bar{g}_{\mu\nu}(x) + \epsilon h_{\mu\nu}(x), \quad |\epsilon| \ll 1, \tag{2.1}$$

where $h_{\mu\nu}$ is the perturbation of the metric and $\bar{g}_{\mu\nu}$ is the Schwarzschild metric, which can be written in Schwarzschild coordinates as

$$ds^2 = -f dt^2 + f^{-1} dr^2 + r^2 d\Omega_2^2, \quad f = f(r) = 1 - \frac{2M}{r}, \tag{2.2}$$

where M is the mass of the BH and $d\Omega_2^2 = d\theta^2 + \sin^2\theta d\phi^2$ is the metric of the 2-sphere. We can see that the spacetime is static, spherically symmetric and asymptotically flat. Schwarzschild coordinates are also known as the area-gauge, since the r-coordinate parametrises the area of spheres with constant r. The perturbations $h_{\mu\nu}$ are assumed to be small enough compared to $\bar{g}_{\mu\nu}$ that linear perturbation theory is adequate [51, 56].

Given that the Schwarzschild metric is invariant under the parity transformation $(\theta, \phi) \to (\pi - \theta, \pi + \phi)$, polar and axial perturbations do not mix when linearising. Under this transformation, spherical harmonics transform as

$$Y_{\ell m}(\pi - \theta, \pi + \phi) = (-1)^\ell Y_{\ell m}(\theta, \phi). \tag{2.3}$$

Accordingly, the polar and axial components of a tensor K transform respectively as

$$K^{\text{pol}} \to (-1)^\ell K^{\text{pol}}, \quad K^{\text{ax}} \to (-1)^{\ell+1} K^{\text{ax}}, \tag{2.4}$$

so that the polar component shares the same parity as the spherical harmonics, whereas the axial component acquires an extra minus sign relative to the spherical harmonics. Therefore, it is natural to decompose the perturbation into a polar (or even) and an axial (or odd) contribution,

$$h_{\mu\nu}(x) = h^{\text{pol}}_{\mu\nu}(x) + h^{\text{ax}}_{\mu\nu}(x). \tag{2.5}$$

Each contribution can be decomposed in terms of tensor spherical harmonics [57], which are solutions to the Laplace equation on the 2-sphere and constitute a complete basis, as [58]

$$h^{\text{pol/ax}}_{\mu\nu}(t, r, \theta, \phi) = \sum_a \sum_{\ell, m} h^a_{\ell m}(t, r) (\mathbf{t}^a_{\ell m})_{\mu\nu}(\theta, \phi), \tag{2.6}$$

where the label a runs over the indices of the tensor harmonics, (ℓ, m) are the multipole and azimuthal numbers respectively, and $(\mathbf{t}^a_{\ell m})_{\mu\nu}$ are the tensor spherical harmonics in spherical coordinates. In addition, we can perform the same decomposition for the energy-momentum tensor,

$$T_{\mu\nu}(x) = T^{\text{pol}}_{\mu\nu}(x) + T^{\text{ax}}_{\mu\nu}(x), \tag{2.7}$$

where the explicit expression for each contribution in terms of the tensor harmonics can be found in Ref. [59].

When considering Einstein equations $G_{\mu\nu} = 8\pi T_{\mu\nu}$, one can expand the Einstein tensor to linear order in $h_{\mu\nu}$,

$$G_{\mu\nu} = \bar{G}_{\mu\nu} + \Delta G_{\mu\nu}, \tag{2.8}$$

and given that the Schwarzschild metric is a solution to Einstein vacuum equations, i.e. it satisfies $\bar{G}_{\mu\nu} = 0$, the perturbations are governed by

$$\Delta G_{\mu\nu} = 8\pi \Delta T_{\mu\nu}, \tag{2.9}$$

where $\Delta T_{\mu\nu}$ is the energy-momentum tensor sourcing the perturbations. There is a particular choice of gauge, first introduced by Regge and Wheeler [51], that allows us to obtain a simplified form for the equations that we want to work with. The RW gauge completely fixes the gauge for $\ell = 2$, i.e. there is no remaining gauge freedom. With this gauge choice, the highest derivatives in the angles θ, ϕ are removed. In this work, we focus on the axial sector, which takes the following form in the Regge-Wheeler gauge [60]

$$h^{\rm ax}_{\mu\nu}(t,r,\theta,\phi) = \begin{pmatrix} 0 & 0 & -h^{(0)}_{\ell m}(t,r)\csc\theta\partial_\phi Y_{\ell m} & h^{(0)}_{\ell m}(t,r)\sin\theta\partial_\theta Y_{\ell m} \\ 0 & 0 & -h^{(1)}_{\ell m}(t,r)\csc\theta\partial_\phi Y_{\ell m} & h^{(1)}_{\ell m}(t,r)\sin\theta\partial_\theta Y_{\ell m} \\ * & * & 0 & 0 \\ * & * & 0 & 0 \end{pmatrix}, \tag{2.10}$$

where $*$ stands for the symmetric elements. The equations for axial perturbations, obtained from the components $(\mu\nu) = (t\phi)$, $(r\phi)$ and $(\theta\phi)$ of equation (2.9), are [59]

$$\partial_r^2 h^{(0)}_{\ell m} - \left(\partial_r + \frac{2}{r}\right)\partial_t h^{(1)}_{\ell m} + \frac{1}{f}\left[\frac{2}{r}\frac{df}{dr} - \frac{\ell(\ell+1)}{r^2}\right] h^{(0)}_{\ell m} = \frac{16\pi}{f} s^{Bt}_{\ell m}, \tag{2.11}$$

$$\partial_t^2 h^{(1)}_{\ell m} - \left(\partial_r - \frac{2}{r}\right)\partial_t h^{(0)}_{\ell m} + f\frac{(\ell-1)(\ell+2)}{r^2} h^{(1)}_{\ell m} = -16\pi\, f s^{B1}_{\ell m}, \tag{2.12}$$

$$\frac{1}{f}\partial_t h^{(0)}_{\ell m} - \partial_r\left[f h^{(1)}_{\ell m}\right] = -16\pi s^{B2}_{\ell m}. \tag{2.13}$$

Note that the first two equations hold for $\ell \geq 1$ while the last one is valid for $\ell \geq 2$. The lower multipoles $\ell = 0, 1$ require a separate treatment [60]. Since vector spherical harmonics exist only for $\ell \geq 1$, and rank-two tensor spherical harmonics only for $\ell \geq 2$, some of the perturbations in the expansion (2.6) vanish for $\ell = 0, 1$, and therefore the equations for these

perturbations should be derived separately [60]. As shown in Appendix G of Reference [58], these low multipoles admit a simple physical interpretation. In the polar sector, the monopole mode $\ell = 0$ describes a perturbation of the BH mass, whereas the dipole mode $\ell = 1$ is pure gauge and corresponds to a displacement of the centre of momentum. In the axial sector, the monopole perturbation vanishes identically, while the dipole mode $\ell = 1$ correspond to a perturbation of the angular momentum of the system, i.e. to the linearized Kerr solution.

As discussed in [59], the gauge invariance implies that these three equations are not independent. It can be shown that, in vacuum, equations (2.12) and (2.13) imply equation (2.11), up to the addition of a time-dependent function to $h^{(0)}_{\ell m}$, which can be fixed by imposing that the BH is unperturbed at $t \to -\infty$. In the presence of a source, the consistency of the three equations is ensured by the covariant conservation of the energy momentum tensor $\bar{\nabla}_\alpha T^{\alpha\beta} = 0$, with respect to the background metric. Then, using equation (2.13) one can eliminate $\partial_0 h^{(0)}_{\ell m}$ from equation (2.12), obtaining an equation for $h^{(1)}_{\ell m}$. Defining the Regge-Wheeler master function

$$\psi_{\ell m}(t,r) = \frac{1}{r}\left(1 - \frac{2M}{r}\right) h^{(1)}_{\ell m}(t,r), \tag{2.14}$$

for $\ell \geq 2$, we get the Regge-Wheeler (RW) equation [51],

$$\left(\frac{\partial^2}{\partial x^2} - \frac{\partial^2}{\partial t^2}\right)\psi_{\ell m} - V^{\rm RW}_\ell(r)\psi_{\ell m} = \mathcal{S}^{\rm ax}_{\ell m}, \tag{2.15}$$

where

$$V^{\rm RW}_\ell(r) = \left(1 - \frac{2M}{r}\right)\left[\frac{\ell(\ell+1)}{r^2} - \frac{6M}{r^3}\right] \tag{2.16}$$

is the Regge-Wheeler potential, and the source term is

$$\mathcal{S}^{\rm ax}_{\ell m} = 16\pi f(r)\left\{f(r)s^{B1}_{\ell m}(t,r) + \left(\partial_r - \frac{2}{r}\right)\left[f(r)s^{B2}_{\ell m}(t,r)\right]\right\}, \tag{2.17}$$

with $s^a_{\ell m}(t,r)$ being the coefficients of the expansion of the energy-momentum tensor in tensor harmonics [59]. Note that x appearing in (2.15) is the tortoise coordinate, defined as

$$f(r)dr = dx \to x = r + 2M\log\left(\frac{2M}{r} - 1\right). \tag{2.18}$$

This coordinate ranges from $x \in (-\infty, \infty)$, with $x \to -\infty$ corresponding to approaching the horizon, and $x \sim r$ far from the horizon.

When considering the polar perturbations, a similar procedure can be followed, obtaining the so-called Zerilli equation [52]. Although the corresponding wave equations involve different

effective potentials, they produce the same set of characteristic frequencies (the quasinormal mode spectrum, to be discussed in the next subsection). In this sense, axial and polar perturbations are isospectral, meaning that they share an identical spectrum and therefore exhibit equivalent dynamical responses at the level of linear perturbations [55].

In the following sections, we drop the subindices $(\ell,\ m)$ in the Regge-Wheeler function to ease the notation.

2.2 RINGDOWN AND BLACK HOLE QUASINORMAL MODES

The evolution of perturbations on a Schwarzschild geometry are governed by the RW and Zerilli equations. The homogeneous solutions to these equations exhibit a characteristic temporal structure: an initial transient, which depends on the details of the perturbation, followed by an intermediate stage dominated by a superposition of exponentially damped oscillations, and finally a late-time power-law tail. A more detailed discussion of these regimes is presented in Section 4.2. In this Section, we focus on the intermediate stage, referred to as the ringdown, which describes how the BH relaxes to its final state after it has been perturbed.

The ringdown phase admits a precise mathematical characterisation in terms of the BH QNMs, which are solutions of the homogeneous perturbation equation that satisfy specific boundary conditions: purely ingoing waves at the event horizon and purely outgoing waves at spatial infinity [59]. These boundary conditions encode the loss of energy to the event horizon and to infinity, and are responsible for the dissipative character of the ringdown signal.

Starting from the time-domain homogeneous RW equation,

$$\left(\frac{\partial^2}{\partial x^2}-\frac{\partial^2}{\partial t^2}\right)\psi(t,x)-V_\ell^{\rm RW}(r)\psi(t,x)=0, \tag{2.19}$$

we can perform a Laplace transform, with parameter $s=-i\omega$, of the RW master function $\psi(t,x)$ as

$$\hat{\psi}(\omega,x)=\int_0^\infty dt\ e^{i\omega t}\psi(t,x), \tag{2.20}$$

where the lower limit $t=0$ reflects the specification of initial data on a Cauchy surface. Note that this expression is analogous to a one-sided Fourier transform. Using this transformation, the homogeneous equation (2.19) becomes

$$\left[\frac{\partial^2}{\partial x^2}+\omega^2-V_\ell^{\rm RW}(x)\right]\hat{\psi}(\omega,x)=\mathcal{I}(\omega,x),\quad \mathcal{I}(\omega,x)=\left[i\omega\psi(t,x)-\frac{\partial\psi(t,x)}{\partial t}\right]\Bigg|_{t=0}, \tag{2.21}$$

where the source term $\mathcal{I}(x)$ depends on the initial conditions at $t = 0$. Let $\hat{\psi}_L(x)$ and $\hat{\psi}_R(x)$ be two linearly independent solution to the homogeneous version of (2.21). These solutions are defined by imposing the previously mentioned boundary conditions. In particular, $\hat{\psi}_L$ behaves as a purely ingoing wave at the horizon, whereas $\hat{\psi}_R$ corresponds to a purely outgoing wave at infinity, namely

$$\hat{\psi}_L(x) = \begin{cases} e^{-i\omega x} & \text{for} \quad x \to -\infty, \\ A_{\text{in}} e^{-i\omega x} + A_{\text{out}} e^{i\omega x} & \text{for} \quad x \to +\infty, \end{cases} \tag{2.22}$$

$$\hat{\psi}_R(x) = \begin{cases} A'_{\text{in}} e^{-i\omega x} + A'_{\text{out}} e^{i\omega x} & \text{for} \quad x \to -\infty, \\ e^{i\omega x} & \text{for} \quad x \to +\infty. \end{cases} \tag{2.23}$$

The solution of the inhomogeneous equation (2.21) can be written in terms of a frequency domain Green's function $\hat{G}(\omega, x, \bar{x})$, defined by

$$\left[\frac{\partial^2}{\partial x^2} + \omega^2 - V_\ell^{\text{RW}}(r)\right] \hat{G}(\omega, x, \bar{x}) = \delta(x - \bar{x}), \tag{2.24}$$

so that the solution to (2.21) is formally given by

$$\hat{\psi}(\omega, x) = \int_{-\infty}^{\infty} d\bar{x}\ \hat{G}(\omega, x, \bar{x}) \mathcal{I}(\omega, \bar{x}). \tag{2.25}$$

In terms of the homogeneous solutions introduced in (2.22) and (2.23), the Green's function takes the form [59]

$$\hat{G}(\omega, x, \bar{x}) = \frac{1}{W(\omega)} \left[\theta(x - \bar{x}) \hat{\psi}_L(\omega, \bar{x}) \hat{\psi}_R(\omega, x) + \theta(\bar{x} - x) \hat{\psi}_L(\omega, x) \hat{\psi}_R(\omega, \bar{x})\right], \tag{2.26}$$

where $\theta(x)$ is the Heaviside step function, and

$$W(\omega) = \hat{\psi}_L(\omega, x)\ \partial_x \hat{\psi}_R(\omega, x) - \hat{\psi}_R(\omega, x)\ \partial_x \hat{\psi}_L(\omega, x) = 2i\omega A_{\text{in}} \tag{2.27}$$

is the Wronskian of $\hat{\psi}_L$ and $\hat{\psi}_R$, which is a constant value depending only on ω. Combining equations (2.25) and (2.26), we can write the solution for $\hat{\psi}(\omega, x)$ as

$$\hat{\psi}(\omega, x) = \hat{\psi}_R(\omega, x) \int_{-\infty}^{x} dx' \frac{\hat{\psi}_L(\omega, x') \mathcal{I}(\omega, x')}{W(\omega)} + \hat{\psi}_L(\omega, x) \int_{x}^{\infty} dx' \frac{\hat{\psi}_R(\omega, x') \mathcal{I}(\omega, x')}{W(\omega)}. \tag{2.28}$$

The time-domain solution $\psi(t, x)$ can be computed by inverting the Laplace transform in (2.20), so that the time-domain solution is

$$\psi(t, x) = \frac{1}{2\pi} \int_{\mathcal{C}} d\omega\ e^{-i\omega t} \hat{\psi}(\omega, x), \tag{2.29}$$

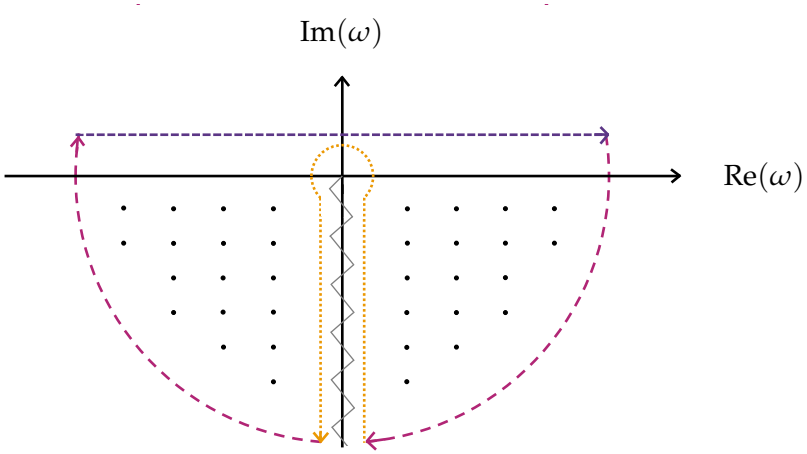

Figure 2.1: Contour integration in the complex frequency plane for the Green's function at sufficiently late times. The black dots represent the simple poles corresponding to the linear QNM frequencies. The branch cut is marked with a grey line.

with $\mathcal{C}$ a contour in the complex $\omega-$plane. The most common choice for $\mathcal{C}$ at sufficiently late times is the integration contour shown in Figure 2.1. It consists of three different parts: a piece above the real axis (purple dashed line), a semicircle (pink dashed line), and a piece surrounding the branch cut and the pole at $\omega = 0$ (orange dotted line). Consequently, the resulting time-domain Green's function can be divided into three separate contributions [43]

$$G(t, x, \bar{x}) = G_F(t, x, \bar{x}) + G_Q(t, x, \bar{x}) + G_B(t, x, \bar{x}). \tag{2.30}$$

where G_F is the contribution coming from the two quarter circles at infinity and the neighbourhood of the branch cut, G_Q comes from the poles inside the contour, and G_B comes from the branch cut. These contributions are known as the flat, QNM, and branch cut contributions, respectively. This structure is further discussed in Section 4.2.

The QNM frequencies correspond to the poles of the Green's function (2.26) or, equivalently, to the values of ω for which the Wronskian vanishes, $W(\omega) = 0$. These frequencies are complex-valued, $\omega \in \mathbb{C}$, and the imaginary part of the frequency describes the dissipation of the system. Using Cauchy's residue theorem and considering the pole contribution to G_Q we can write the ringdown signal as a superposition of damped oscillations [33, 43]

$$\psi_Q(t, x_r) = \sum_{n=0}^{N} A_n e^{-i\omega_n (t - t_{\text{peak}})} \tag{2.31}$$

where x_r is the extraction radius, $A_n \in \mathbb{C}$ is the amplitude of $n-$th mode, $\omega_n \in \mathbb{C}$ is the frequency of the mode n, and t_{peak} is some reference time, which we choose to be the peak of the signal. Both the amplitude and the frequency are complex, and depend on the azimuthal

numbers of the perturbation ℓ, m. The longest lived mode, identified by having the smallest imaginary part of its frequency, is called the fundamental mode. The remaining modes, ordered by increasing damping rate, are called the overtones and are labelled by the subindex n.

The QNM frequencies can be computed numerically as the poles of the Green's function. The corresponding QNM amplitudes can be written as [45]

$$A_n = B_n \int_{-\infty}^{\infty} dx' \frac{\mathcal{I}(\omega, x')\psi_L(\omega, x')}{A_{\text{out}}}, \tag{2.32}$$

where

$$B_n = \frac{A_{\text{out}}}{2\omega} \left(\frac{dA_{\text{in}}}{d\omega} \right)^{-1} \Bigg|_{\omega=\omega_n} \tag{2.33}$$

are the quasinormal mode excitation factors (QNEFs). While the QNEFs depend only on the background geometry, equation (2.32) shows that the amplitudes also depend on the initial perturbation $\mathcal{I}(\omega, x)$. Therefore, the amplitudes can be predicted only when the source of the perturbation is known. In realistic observational scenarios, however, the initial perturbation is not known, and thus the amplitudes must be instead inferred directly by fitting the ringdown signal to QNMs.

2.3 THE LIGHT RING

In the high-frequency limit, GWs propagate at the speed of light along null geodesics of the background spacetime. This follows directly from the linearised Einstein equations in vacuum [61],

$$\bar{\Box} h_{\mu\nu} + 2\bar{R}_{\alpha\mu\beta\nu} h^{\alpha\beta} = 0, \tag{2.34}$$

where $\bar{\Box} = \bar{\nabla}_\mu \bar{\nabla}^\mu$ is the D'Alembertian operator over the background metric. This equation is written in the Lorenz gauge $2\bar{\nabla}^\mu h_{\mu\nu} = \bar{\nabla}_\nu h$, where $\bar{\nabla}_\mu$ denotes the covariant derivative with respect to the background metric and h is the trace of the perturbation.

In the geometric optics limit $\lambda \ll K$, where λ is the wavelength of the perturbation and K is the curvature scale of the background, we introduce the ansatz

$$h_{\mu\nu} = \text{Re}\left[A_{\mu\nu}(x) e^{i\theta(x)/\epsilon} \right], \tag{2.35}$$

where $\epsilon \ll 1$ is a bookkeeping parameter, $A_{\mu\nu}$ is a slowly varying amplitude, and $\theta(x)$ is a rapidly varying phase. The wave vector is defined as $k_\mu \equiv \bar{\nabla}_\mu \theta$, the leading-order contributions $\mathcal{O}(\epsilon^{-2})$ of equation (2.34) yield

$$\bar{g}_{\mu\nu} k^\mu k^\nu = 0, \quad k^\mu \bar{\nabla}_\mu k_\nu = 0. \tag{2.36}$$

These equations show that, at leading-order, high-frequency GWs follow null geodesics of the background spacetime. Let us thus study null geodesics on the Schwarzschild geometry.

In Schwarzschild spacetime, the spherical symmetry allows restricting the motion of geodesics to the equatorial plane $\theta = \pi/2$, $\dot{\theta} = 0$ without loss of generality. The components of a tangent vector $\dot{x}^\mu$ to a curve x^μ parametrised by τ are $\dot{x} = dx^\mu/d\tau$, so that null geodesics satisfy

$$0 = -f(r)\dot{t}^2 + f^{-1}(r)\dot{r}^2 + r^2\dot{\phi}^2. \tag{2.37}$$

This equation can be written in the form of a one-dimensional mechanical system

$$\frac{1}{2}\dot{r}^2 + V_{\text{eff}} = \frac{E^2}{2}, \quad V_{\text{eff}} = \frac{L^2}{2r^2} f(r), \tag{2.38}$$

where V_{eff} is an effective potential, and $E = f(r)\dot{t}$, $L = r^2\dot{\phi}$ are the conserved quantities, interpreted as the energy and angular momentum of a photon, associated to the time translation and axial symmetries of the spacetime.

The potential has a single maximum located at $r_{\text{LR}} = 3M$ ($x_{\text{LR}} \simeq 1.61M$), and it is independent of the angular momentum L. This corresponds to an unstable circular orbit of photons [61]. In Schwarzschild spacetime, this orbit forms a two-sphere of radius r_{LR}, referred to as the photon sphere or light ring. In Figure 2.2 we plot the normalised effective potential for null geodesics together with the RW potential for perturbations with $\ell = 2, 3, 4$. As the azimuthal number increases, the RW potential approaches the effective potential for null-geodesics, so that in the eikonal limit ($\ell \gg 1$) the two coincide, since in this limit the RW potential behaves as

$$V_\ell^{\text{RW}}(r) \approx \ell^2 \frac{f(r)}{r^2} \propto V_{\text{eff}}, \tag{2.39}$$

so it peaks at the light ring, similarly to the effective potential for null geodesics. Therefore, in the eikonal limit, the light ring becomes relevant to BH perturbations.

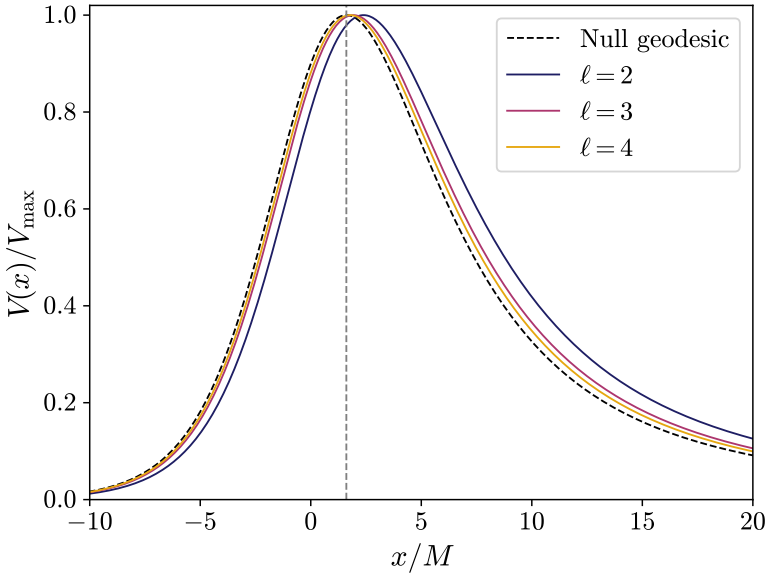

Figure 2.2: Normalised effective potential for null geodesics (black dashed line) together with the Regge-Wheeler potential (2.16) for perturbations with azimuthal numbers $\ell = 2, 3, 4$, plotted as functions of the tortoise coordinate x. The vertical, grey line shows the position of the light ring, $x_{\rm LR} = 1.61M$.

As explained in Section 2.2, QNMs are defined by purely ingoing boundary conditions at the horizon and purely outgoing conditions at infinity. In a Wentzel-Kramers-Brillouin (WKB) treatment [62–64], one can approximate the potential near its maximum $x = x_{\rm LR}$ as [65, 66]

$$V_\ell^{\rm RW}(x) = V_0 + \frac{1}{2}V_0''(x - x_{\rm LR})^2 + \mathcal{O}(x^3), \tag{2.40}$$

so that the problem reduces locally to an inverted harmonic oscillator. Matching the WKB solutions across the turning points of the approximation, so that they satisfy the boundary conditions, yields the Bohr-Sommerfeld quantisation condition [65]

$$\frac{i(\omega^2 - V_0)}{\sqrt{-2V_0''}} = n + \frac{1}{2}, \quad n = 0, 1, 2\ldots \tag{2.41}$$

In the eikonal limit and using equation (2.39), the quantities V_0 and V_0'' can be expressed in terms of properties of the light ring as [67]

$$V_0 = \ell^2\Omega_c^2, \quad \sqrt{-\frac{V_0''}{2V_0}} = |\lambda|, \tag{2.42}$$

where Ω_c is the frequency of the light ring and λ is the Lyapunov exponent[1], which measures the instability timescale of radial perturbations of the orbit [67]. Substituting these expressions into the Bohr-Sommerfeld condition (2.41) gives

$$\omega_{\rm QNM} = \Omega_c \ell - i\left(n + \frac{1}{2}\right)|\lambda|. \tag{2.43}$$

This result is, strictly speaking, only valid in the eikonal regime, since it relies on WKB approximations. However, it yields surprisingly accurate predictions even for low values of ℓ [65, 67]. It can be physically interpreted as follows. The real part of the frequency, $\mathrm{Re}(\omega_{\rm QNM}) = \Omega_c \ell$ corresponds to waves orbiting the BH at the light-ring frequency, while the imaginary part $\mathrm{Im}(\omega_{\rm QNM}) = -(n+1/2)|\lambda|$ is set by the instability rate of the null orbit. Hence, in the eikonal limit QNMs can be understood as null particles (radiation) trapped near the light ring and leaking away on the Lyapunov timescale [67, 68]. Consequently, essential features of the QNMs are fixed by spacetime properties around the light ring, and the ringdown carries imprints of light-ring physics [33].

[1]The Lyapunov exponent is a measurement of the convergence or divergence of nearby trajectories in the phase space [67]. A positive (negative) Lyapunov exponent indicates a divergence (convergence) between nearby trajectories or, in other words, a higher (lower) sensitivity to initial conditions.

3

METHODS

Within this framework, we want to study the evolution of an initial perturbation in vacuum (Section 4) and in the presence of a source (Section 5). In particular, we want to study how the amplitudes of the QNMs depend on our choice of initial conditions. To this end, we need to obtain the numerical solutions to the RW equation. In this Section, we describe the methods used to integrate numerically the time-domain RW equation (2.15), as well as the convergence test done on the code to check its accuracy. Finally, we discuss the matrix pencil method, which we use to extract the amplitudes of the QNMs from the numerical signals.

3.1 TIME-DOMAIN EVOLUTION OF THE REGGE-WHEELER EQUATION

We use the method of lines to solve numerically the RW equation (2.15). It allows us to transform the partial differential equation that we aim to solve into a set of coupled ordinary differential equations at each point of the grid. We evolve in time using a explicit fourth-order Runge-Kutta scheme (RK4). As for the derivatives, we use a fourth-order finite difference approximation for both the first- and second-order derivatives. These approximations satisfy summation by parts, which helps to achieve numerical stability [69]. Moreover, to avoid noise coming from high frequency modes that can grow in time at a fixed resolution, we also add Kreiss-Oliger dissipation to the algorithm [70].

We impose boundary conditions that enforce that the wave is purely ingoing at the horizon (inner boundary of the grid) and purely outgoing at infinity (outer boundary of the grid). Since we are using numerical methods to integrate the equation, these boundary conditions are only approximate, so there are some spurious reflections at the edges of the grid. To prevent this numerical noise from contaminating the signal, we place the boundaries of interest far enough so that the reflected wave cannot interfere with the scattered wave in the time interval that we consider.

For our simulations, we set $(x_{\min}, x_{\max}) = (-150M, 350M)$ for the spatial grid and evolve the initial wave packet until the final time $t_{\max} = 400M$. When choosing the resolution of the grid, we need to consider how wide the Gaussians we are going to work with as initial conditions are. In order to resolve sufficiently small spatial features, we choose a grid spacing of $\Delta x = 0.005M$. To ensure convergence when solving numerically the differential equation, we implement the Courant–Friedrichs–Lewy condition, which sets an upper boundary for the time step Δt. We set $\Delta t = 0.5\Delta x$, thus ensuring the stability of the method. We extract the signal at three points of interest in the grid: close to the horizon ($r = 2.099M$), at the light ring ($r = 3.000M$), and far from the BH ($r = 125M$).

3.2 CONVERGENCE ANALYSIS

We have tested the accuracy of the algorithm used to solve the RW equation by performing a convergence analysis, analogous to the one carried out in [71]. When using finite differencing, the numerical results ψ_{num} differ from the continuous ones ψ_{cont} by an error that has a polynomial dependence on the resolution, so that $\psi_{\text{cont}} = \psi_{\text{num}} + \mathcal{O}\left((\Delta x)^p\right)$, where Δx is the resolution of the grid and p is the order of accuracy. The order N depends on the numerical implementation. The convergence of the code can be evaluated by running simulations with the same configuration of parameters with coarse, medium, and fine resolutions, labelled as Δx_c, Δx_m and Δx_f respectively. Normally, one assumes a uniform refinement for the grid, typically $\Delta x_c = 4\Delta x_f$ and $\Delta x_m = 2\Delta x_f$, so that the order of accuracy p can be computed as

$$p = \log_2 \left(\frac{\psi_c - \psi_m}{\psi_m - \psi_f} \right), \tag{3.1}$$

where ψ_i is any of the evolved variables obtained for resolution Δx_i for a given instant of time.

In our case, we perform the test for a simulation with fixed parameters $\ell = 2$, $\sigma = 1.0$ and $x_0 = 30.0$, and we use the signal extracted at infinity ($r = 125M$). For the resolutions, we run the test for $\Delta x_c = 0.0100M$, $\Delta x_m = 0.0050M$ (our working resolution) and $\Delta x_f = 0.0025M$. As mentioned above, our code uses an RK4 method to solve the equation numerically, with fourth-order finite difference approximations for the derivatives. The boundary conditions that we are imposing are only first-order approximations. However, for the convergence analysis we are working in an interior region, it is the fourth-order truncation error that dominates. Hence, we expect our simulation to have fourth-order accuracy ($p = 4$). Figure 3.1 shows the results of the convergence analysis for the resolutions specified above. It shows fourth order convergence in the whole evolution, as expected. For $t > 240M$ the signals start to differ, but when this

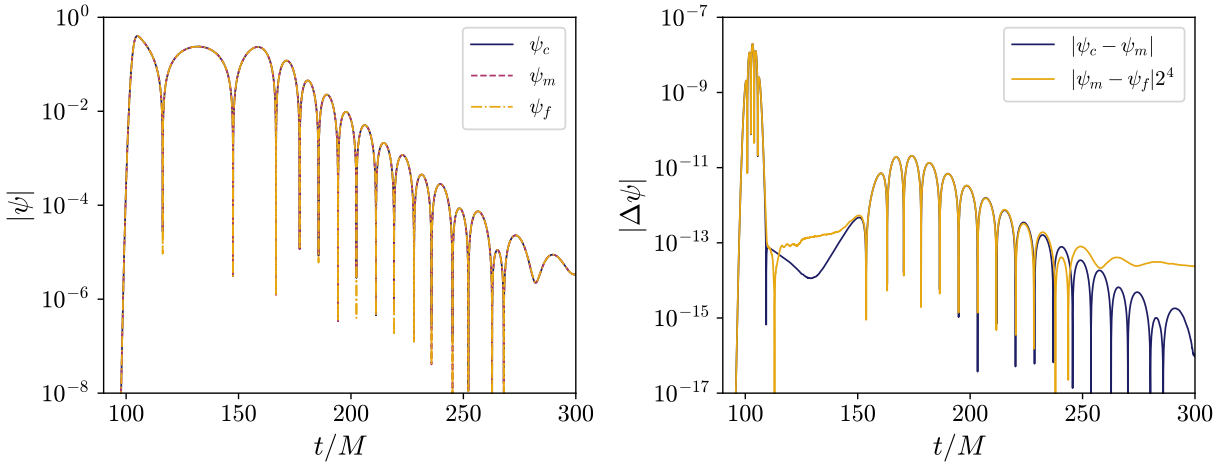

Figure 3.1: Convergence analysis of the numerical solution to the Regge-Wheeler equation (2.15) for $\ell = 2$ perturbations with initial conditions IC1 (introduced later in (4.1)), with $\sigma = 1.0$ and $x_0 = 30.0$. We show the differences between the coarse and medium resolutions, and between the medium and fine resolutions, with the latter rescaled by $2^4 = 16.0$ to assess convergence order. Fourth-order convergence is observed throughout the signal, with the exception of late times, where the deviation is attributed to numerical noise.

begins to happen the error between the different signals is approximately 10^{-13}. Therefore, this discrepancy is likely due to round-off errors and loss of significance in floating-point arithmetic, i.e. in this regime the signal is dominated by numerical noise and has no physical meaning.

3.3 FITTING METHODS

The main part of our analysis relies on extracting the amplitudes of the QNMs from the obtained signals for different combinations of parameters of the initial data. The QNM frequencies are predicted by GR, and they do not depend on the initial conditions. Therefore, we can fix them to the tabulated values [72], shown in Table 3.1, and fit only the QNM amplitudes.

The model that we use for the fitting is given by the approximation in (2.31), in which we consider only the fundamental mode and two, so that $N = 2$. Therefore, we approximate the ringdown signal by

$$y_{\text{fit}}(t) = A_0 \cos\left[-i\omega_0(t - t_{\text{peak}})\right] + A_1 \cos\left[-i\omega_1(t - t_{\text{peak}})\right] + A_2 \cos\left[-i\omega_2(t - t_{\text{peak}})\right], \quad (3.2)$$

with ω_i in Table 3.1. Hence, the parameters that we are fitting for are the amplitudes A_n, which are complex numbers, as explained in Section 2.2.

Fixing the frequencies allows the code to be both faster and more robust. The method we use to extract the amplitudes is the generalised pencil-of-function method or matrix pencil

	ωM	
n	$\ell = 2$	$\ell = 4$
0	0.37367 - 0.08896i	0.80917 - 0.09416i
1	0.34671 - 0.27391i	0.79663 - 0.28433i
2	0.30105 - 0.47827i	0.77270 - 0.47990i

Table 3.1: Frequencies for the fundamental mode and the first two overtones for a gravitational perturbation, tabulated in [72]. Accurate to the decimal digits shown.

method (MPM) [73]. This method assumes that the data are well described by a finite sum of exponentials, as shown in equation (2.31). This series is embedded into a matrix, so that the exponential structure becomes an algebraic structure, and using shift invariance we transform the problem into an eigenvalue problem, which corresponds to computing the QNM frequencies. The details related to the MPM can be found in Appendix A. For our calculations, we choose the matrix pencil to be $L = 3$, since we are fitting for the fundamental mode and two overtones.

If the QNM frequencies are already fixed, the problem becomes linear on the amplitudes, so we no longer have to solve an eigenvalue problem. Instead, we compute the amplitudes via the Moore-Penrose pseudoinverse, using the singular value decomposition. This method allows to obtain stable amplitudes and control truncation, allowing for a fast, stable, and initialisation-free implementation. To get a measurement of the quality of a fit, we define the mismatch between the data y and the fit $y_{\rm fit}$ as

$$\mathcal{M} = 1 - \frac{\langle y|y_{\rm fit}\rangle}{\sqrt{\langle y|y\rangle\,\langle y_{\rm fit}|y_{\rm fit}\rangle}}, \tag{3.3}$$

where the symbol $\langle\cdot|\cdot\rangle$ denotes the product defined as

$$\langle f|g\rangle = \int_{t_0}^{t_{\rm end}} dt' f(t')g(t') \tag{3.4}$$

We test our fitting function by performing fits including a different number of overtones for two sets of data, generated from initial conditions with $\sigma = 2.0M$ and $\sigma = 4.0M$, and $x_0 = 30.0M$ in both cases. The initial conditions are of the form IC1, which are later introduced in equation (4.1). We consider fitting windows with $(t_0, t_{\rm end}) = (5M, 60M)$, so that we consider only the signal before the appearance of the tail. The results are shown in Figure 4.3. In these plots, we observe that for the data corresponding to $\sigma = 2.0M$ the mismatch decreases by approximately one order of magnitude by every overtone we add to the fit. In the case of the data corresponding to $\sigma = 4.0M$, this behaviour is only observed until $N = 2$; adding the third overtone does not improve the fit as much as in the other case. This is related to the fact that

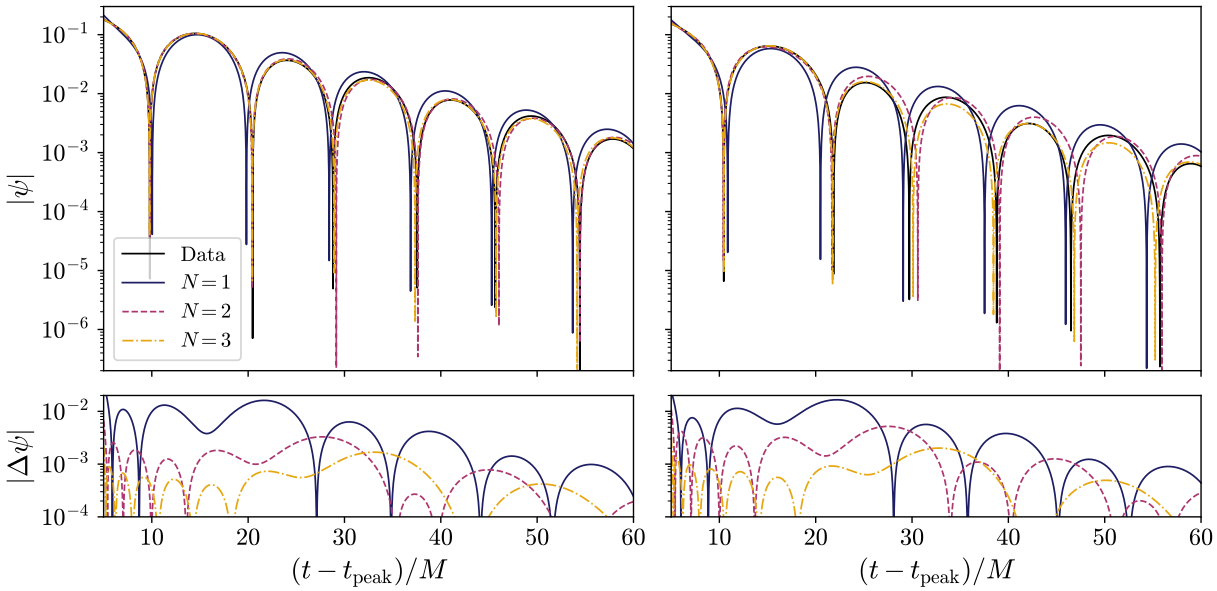

Figure 3.2: Ringdown fits using an increasing number of overtones for two datasets generated by initial condition IC1 with $\sigma = 2.0M$ (left) and $\sigma = 4.0M$ (right), both $x_0 = 30.0M$ and $\ell = 2$. The lower panels show the residuals between each fit and the data. The fitting window $(t - t_{\rm peak}) \in [5M, 60M]$ is chosen to exclude the late-time tail contribution.

we fit both data in the same window, but for larger values of σ the tail starts to interfere with the data sooner, as we discuss in Section 4.2.3. Therefore, the fits for $\sigma = 4.0M$ are worse than for $\sigma = 2.0M$ because in the former we should reduce the fitting window to $t_{\rm end} \approx 50M$, so that the effects caused by the interference with the tail are reduced.

4

INITIAL-VALUE PROBLEM

We begin by considering the homogeneous RW equation (2.19). This approach allows us to study the intrinsic response of the BH, and it is the cleanest way to study QNM excitation. In this Section we study the structure of the signal obtained numerically, to later on study the dependence of QNM excitation of the parameters of the initial data, namely the width and the position. In Section 4.1, we introduce the two sets of initial conditions that are used to solve the equation. In Section 4.2 we study the structure of the time-domain numerical solutions, relating it to the structure of the Green's function. In Section 4.3, we study overtone excitation by examining the behaviour of the amplitudes of the fundamental mode as function of the fitting window, as well as the Gaussian width and location.

4.1 INITIAL CONDITIONS

We solve numerically the RW equation (2.15) for a massless field ψ. To do this, we need to impose appropriate initial conditions. We study two sets of initial conditions,

$$\textbf{IC1}: \quad \psi|_{t=0} = 0 \quad \text{and} \quad \partial_t \psi|_{t=0} = \frac{1}{\sigma\sqrt{2\pi}} \exp\left[-\frac{(x-x_0)^2}{2\sigma^2}\right], \tag{4.1}$$

$$\textbf{IC2}: \quad \psi|_{t=0} = \frac{1}{\sigma\sqrt{2\pi}} \exp\left[-\frac{(x-x_0)^2}{2\sigma^2}\right] \quad \text{and} \quad \partial_t \psi|_{t=0} = 0, \tag{4.2}$$

where σ is the width of the Gaussian pulse and x_0 is its initial position. We perform a time-evolution and extract the time-domain signal close to the horizon, at the light ring and far from the BH.

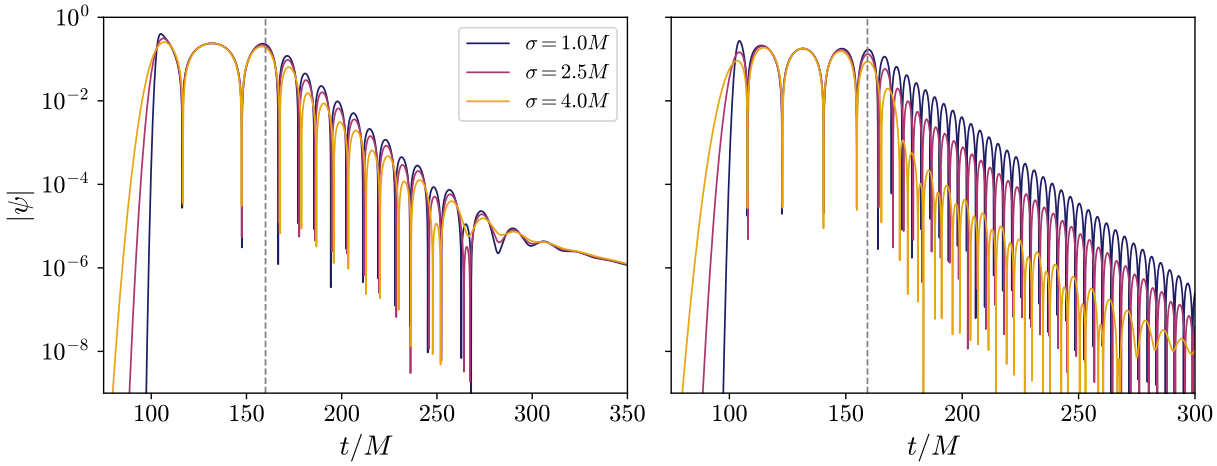

Figure 4.1: Ringdown signals extracted at $r = 125M$ for initial conditions IC1 with $x_0 = 30.0$ and varying σ. On the left (right) panel we plot the signal produced by a perturbation with $\ell = 2$ ($\ell = 4$). The vertical dashed line marks the peak of the waveform, separating the prompt response (left) from the ringdown and power-law tail (right).

4.2 DISSECTING RINGDOWN

We begin by examining the signals obtained by numerically solving the RW equation, and we focus on understanding their structure. Figure 4.1 shows some of the signals we have obtained using our algorithm. Note that we are plotting the absolute value of the signal in logarithmic scale, in order to see better the damping and the oscillations. The signals can be divided into three parts: the prompt response, the ringdown, and the power-law tail, which appears at late times. This structure can also be inferred from studying the Green's function.

As discussed in Section 2.2, the time-domain Green's function can be decomposed into three contributions, according to equation (2.30). These contributions are known as the flat, QNM, and branch cut contributions, respectively. We discuss each of the three parts of the signal, as well as their connection to the components of the Green's function, separately.

4.2.1 *Prompt response*

The first part of the signal corresponds to the left of the grey dashed line in Figure 4.1, and is known as the prompt response of the BH. Historically, it has been expected to be ruled by G_F in (2.30), with information of asymptotically far signals [33]. In particular, the prompt response was thought to originate from the two high-frequency quarter circles of the frequency domain Green's function [41, 43]. However, in [74] it is argued that the contribution of these high-frequency arcs vanishes as a result of Jordan's lemma. This work also shows that the

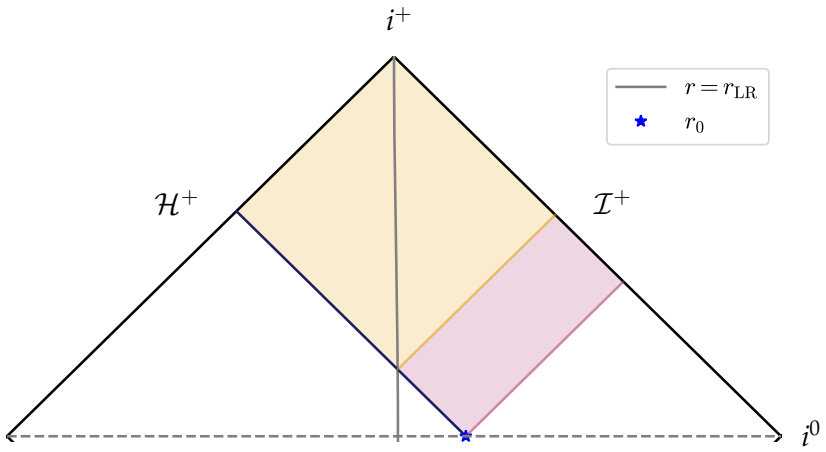

Figure 4.2: Penrose diagram of the exterior region of a Schwarzschild BH. The grey line indicates the location of the light ring. The blue curve marks the trajectory of a perturbation propagating at the speed of light, whose initial position is marked with a star. The pink (yellow) region correspond to the portion of the signal reaching an observer at future null infinity, namely the prompt response (QNMs and late-time tail) contribution.

prompt response signal actually arises from the poles at $\omega = 0$ in the frequency domain, being rather a small-frequency response.

For causality reasons [33, 59], for $t < x - x_0$, where x_0 is the position of the initial data, no signal has yet reached the observer. At $t \approx x - x_0$, the part of the initial perturbation that was moving outwards arrives to the observer, which is propagated by G_F. We observe this prompt response as the main contribution in the signal until the scattered contribution, which comes from the QNMs of the BH, arrives at $t \approx x + x_0$, as shown in Figure 4.2. Therefore, the prompt response lasts for $t_{\rm prompt} = 2x_0$. Note that all of these features depend only on the position of the initial data, so the prompt response ends and has roughly the same duration for all the values of σ. This is precisely what we observe in both panels of Figure 4.1.

If we now look at the structure of the prompt response in Figure 4.1, we can see that it has exactly ℓ zeros, being ℓ the multipole number. This matches with the prediction made in Ref. [74], in which it is derived that the analytical expression of the prompt response of a Schwarzschild BH is a polynomial of order ℓ in the observer's retarded time. Note that this is the structure we observe for signals generated using IC1, which are ingoing. Were we to use IC2 instead, we would observe an extra peak in the prompt response, and therefore one extra zero. This extra peak accounts to the initial condition propagating directly towards the observer, since the initial conditions IC2 are initially static and thus, when the evolution starts, it moves both towards the BH and the observer.

4.2.2 *Ringdown signal*

The second part corresponds to the ringdown signal, which begins at the grey dashed line in Figure 4.1. We can see that this part is characterised by exponentially damped sinusoids and is ruled by G_Q in equation (2.30). This contribution comes from the sum over the residues at the linear QNM frequency poles, as previously discussed in Section 2.2.

In Figure 4.1, we can see that for $\ell = 4$ and larger values of σ, specifically for $\sigma = 4.0M$, the signal is deformed with respect to the other two. In particular, we see that a beating pattern appears in the oscillations, together with a small deviation from a single exponential. This behaviour seems to appear at a critical value for σ, which is smaller for larger multipole numbers. It has been argued that, for scalar perturbations, there is a critical value for the width of the Gaussian in the initial data for which the fundamental mode is maximally excited, which is [75]

$$\sigma^{\text{scalar}}_{\ell,\text{crit}} = \frac{12.24M}{\ell + 1/2}. \tag{4.3}$$

For initial data wider than this, the fundamental mode becomes exponentially suppressed, so that the (possible) interference of the modes becomes more visible, due to their higher amplitudes. This behaviour was also discussed in [47]. It is reasonable to expect a similar behaviour for gravitational perturbation. Hence, we postulate that, for gravitational perturbations, there also exists a value of the Gaussian width for which the fundamental mode is maximally excited, in particular

$$\sigma^{\text{grav}}_{\ell,\text{crit}} = \frac{KM}{\ell + 1/2}, \tag{4.4}$$

where K is some dimensionless, numerical constant. According to this expression, for perturbations with $\ell = 2, 4$ and using equation (4.4), we expect

$$\frac{\sigma_{2,\text{crit}}}{\sigma_{4,\text{crit}}} = \frac{4 + 1/2}{2 + 1/2} = 1.8. \tag{4.5}$$

We can check this prediction for the behaviour observed in the signals and described above. By generating several simulations for multiple values of σ, we can get an eye-estimate of the value of the Gaussian width for which the beating pattern starts to become visible. In particular, we observe a value of $\sigma_{2,\text{obs}} \approx 5M$ for $\ell = 2$, and $\sigma_{4,\text{obs}} \approx 3.5M$. Using these estimations, we obtain $\sigma_{2,\text{obs}}/\sigma_{4,\text{obs}} \approx 1.4$, which agrees very well with the prediction in equation (4.5).

For our analysis, we are interested in fitting and extracting the amplitudes of some QNMs during the ringdown part of the signal. Therefore, for the calculations we carry out in the rest

of the thesis we focus only on the region to the right of the grey dashed line in Figure 4.1, before the appearance of the power-law tail.

4.2.3 *Power-law tail*

The third and last part of the signal corresponds to a power-law behaviour, known as the late-time tail or Price tail [43, 76]. In the Green's function decomposition (2.30), this contribution is associated with G_B and arises from the branch cut contribution in the frequency domain. Physically, it is understood to arise from the backscattering of waves off the spacetime curvature, more precisely from the long-range part of the effective potential, which generates non-negligible scattering even at asymptotically late times and low frequencies [33]. In fact, it has been shown that the tails are absent from the signal if the potential has compact support or if it decays exponentially [59]. Moreover, the existence of tails is only dictated by the asymptotic form of the potential, rather than its local structure, and, in particular, it is independent of the presence of horizons in the metric [77, 78]. As a result of the long-range potential, the radiation that propagates outwards is partially scattered back towards the observer by the curvature of spacetime itself, producing a slowly decaying time at late times. The behaviour observed at a fixed spatial position at very late times for the massless field is $\Phi \sim t^{-p}$, $p = 2\ell + 3$ for non-static initial field and $p = 2\ell + 2$ for static initial field, where $\Phi = \psi(t, r)Y_{\ell m}/r$ [59, 76].

The onset of the tail depends sensitively on the properties of the initial perturbation. It appears earlier for wider initial conditions and lower multiple numbers. This early onset also contributes to the appearance of a beating pattern, as observed in the right panel of Figure 4.1 for the largest values of σ, which corresponds to the interference between QNMs and the tail. Given that the fundamental mode is suppressed for such values of σ, as discussed in Section 4.2.2, this interference becomes more visible. In [79] it is argued that late-time power-law tails can be approximated by purely damped exponentials over a finite interval, which can interfere with the QNMs, hence generating the beating patterns. This is further investigated in Appendix **??**. Moreover, the curvature that the signal acquires in the decay, which can be observed in Figure 4.1 for $\ell = 4$, $\sigma = 4.0M$, is related with the late-time power-law tail.

The dependence of the signal on the initial data can be understood in terms of its spectral content. Narrow Gaussian profiles contain a broad Fourier spectrum, so when used as initial data they tend to excite many overtones. On the other hand, wide Gaussians contain a narrow Fourier spectrum concentrated at low frequencies, and therefore only the QNMs whose real parts lie in the spectral window get appreciable excitation, i.e. less overtones are excited, since

their frequencies are smaller than the fundamental mode. Hence, for wide initial data, the fundamental mode is exponentially suppressed and the overtones are hardly excited, which allows an early onset of the tail and its interference with the QNMs. If the Gaussian is wide enough, there is hardly any ringing at all. This was first observed and discussed in 1970 [53], and it has also been discussed in more recent works [44, 46, 75].

4.3 MODE CONTENT

Once we can extract the amplitudes of the QNMs from the ringdown signals, we can study their dependence on the beginning of the fitting window, t_0, and on the initial data. In particular, we study the dependence of the amplitudes on the parameters of the Gaussian in IC1 and IC2, namely the width σ and the initial position x_0. To this end, we must consider that the peak of the signal also depends on the initial condition, as can be seen in Figure 4.1. Consequently, in our analysis we divide the amplitudes of the QNMs extracted from the fits by the amplitude of the peak of the signal, as a way of normalising the data.

4.3.1 *Dependence on the fitting window*

We begin by analysing the behaviour of the amplitudes as a function of t_0, which denotes the starting time of the fitting window, while keeping t_{end} fixed. Figure 4.3 shows the amplitudes of the modes for three different fitting models, each of them including a different number of modes.

As a validation step, we verify that our results are consistent with those reported in Ref. [48]. We observe that the amplitudes A_0 and A_1 exhibit approximate stability over a finite interval of t_0. This behaviour enables a reliable determination of these amplitudes by averaging over the corresponding interval. In contrast, higher overtones do not display this trend. Instead, their extracted amplitudes increase with t_0, indicating a strong sensitivity to the choice of the fitting window. This behaviour suggests that these amplitudes cannot be determined with enough confidence within our current setup. For this reason, the remainder of our analysis focuses only on the fundamental and first excited modes, which can be consistently and confidently excited for both $\ell = 2$ and $\ell = 4$. Accordingly, we restrict our attention to fits with $N = 2$, which include the fundamental mode and the two first overtones.

In Figure 4.3, we further observe that the amplitudes corresponding to the modes with $\ell = 4$ (dashed lines) exhibit greater stability than those with $\ell = 2$ (solid lines). In the case $\ell = 4$, the

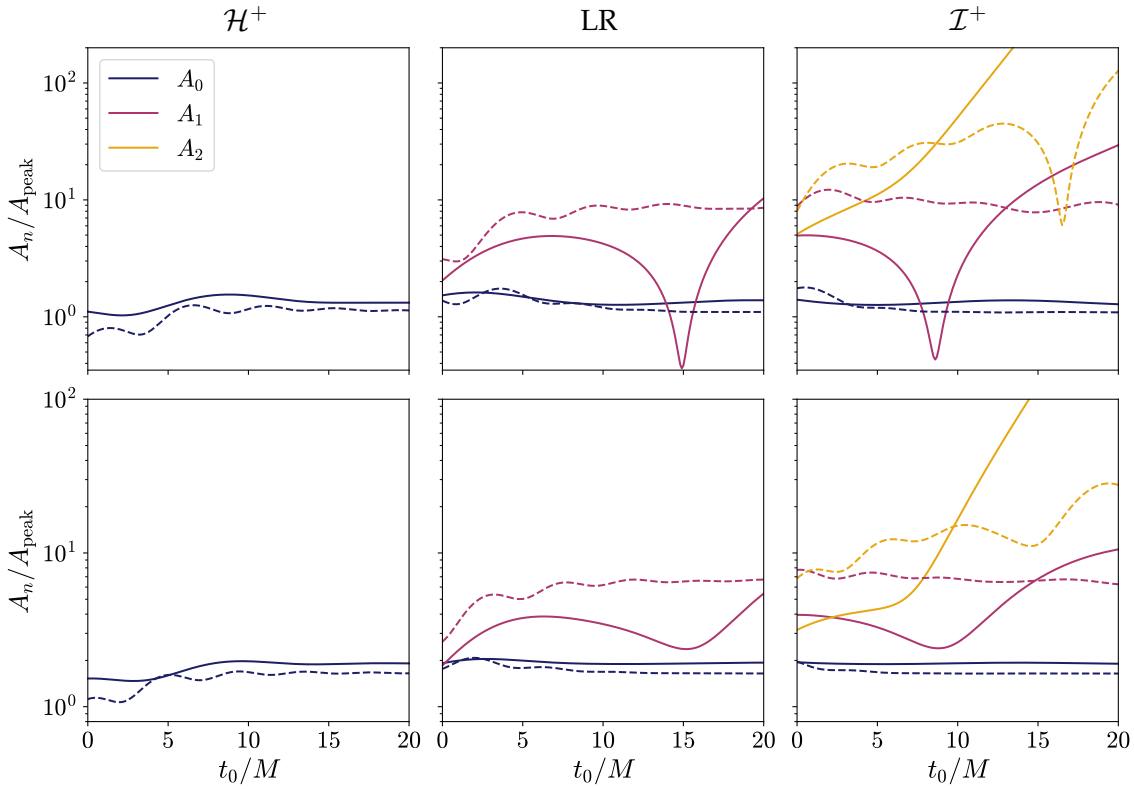

Figure 4.3: QNMs amplitudes from fits to data generated by an initial condition with $\sigma = 1.0M$ and $x_0 = 30.0M$, extracted at infinity. The top (bottom) row corresponds to IC1 (IC2). Solid (dashed) lines correspond to by perturbations with $\ell = 2$ ($\ell = 4$). Note that the y-axis scale differs between rows; the x-axis is common to all panels.

ringdown oscillations occur at higher frequencies and are therefore narrower as function of time, as illustrated in Figure 4.1. Consequently, within a fixed fitting window a larger number of cycles can be included in the fit, leading to improved accuracy and enhanced stability of the extracted amplitudes. Moreover, the peak observed for $\ell = 2,\ n = 1$ mode in the first row of panels can be attributed to interference effects with additional overtones.

Based on the results in Figure 4.3, we determine an appropriate fitting window for extracting the QNM amplitudes. We fix the upper bound of the fitting window at $t_{\text{end}} = 80M$, and consider fitting intervals of the form $(t_0, t_{\text{end}}) = (t_0, 80M)$. For each choice of of initial data parameters, namely σ and x_0, we perform a series of fits by varying $t_0 \in [0, 20M]$, following the same procedure adopted in Figure 4.3. To determine the amplitudes, we identify a subinterval $[t_1, t_2] \subset [0, 20M]$ over which the amplitudes display a stable behaviour. This stability window changes for each combination of initial data parameters, but it typically around $5M - 7M$ wide. However, in all cases we impose the condition $t_2 < 10M$, ensuring that the first overtone is still present in the signal. The associated uncertainty to the amplitude is then estimated as the standard deviation of the amplitudes computed within the selected stability window. For the following, we do not include the amplitude corresponding to the second overtone A_2 in the plots, since the stability window for this mode is too small to extract it with enough confidence,

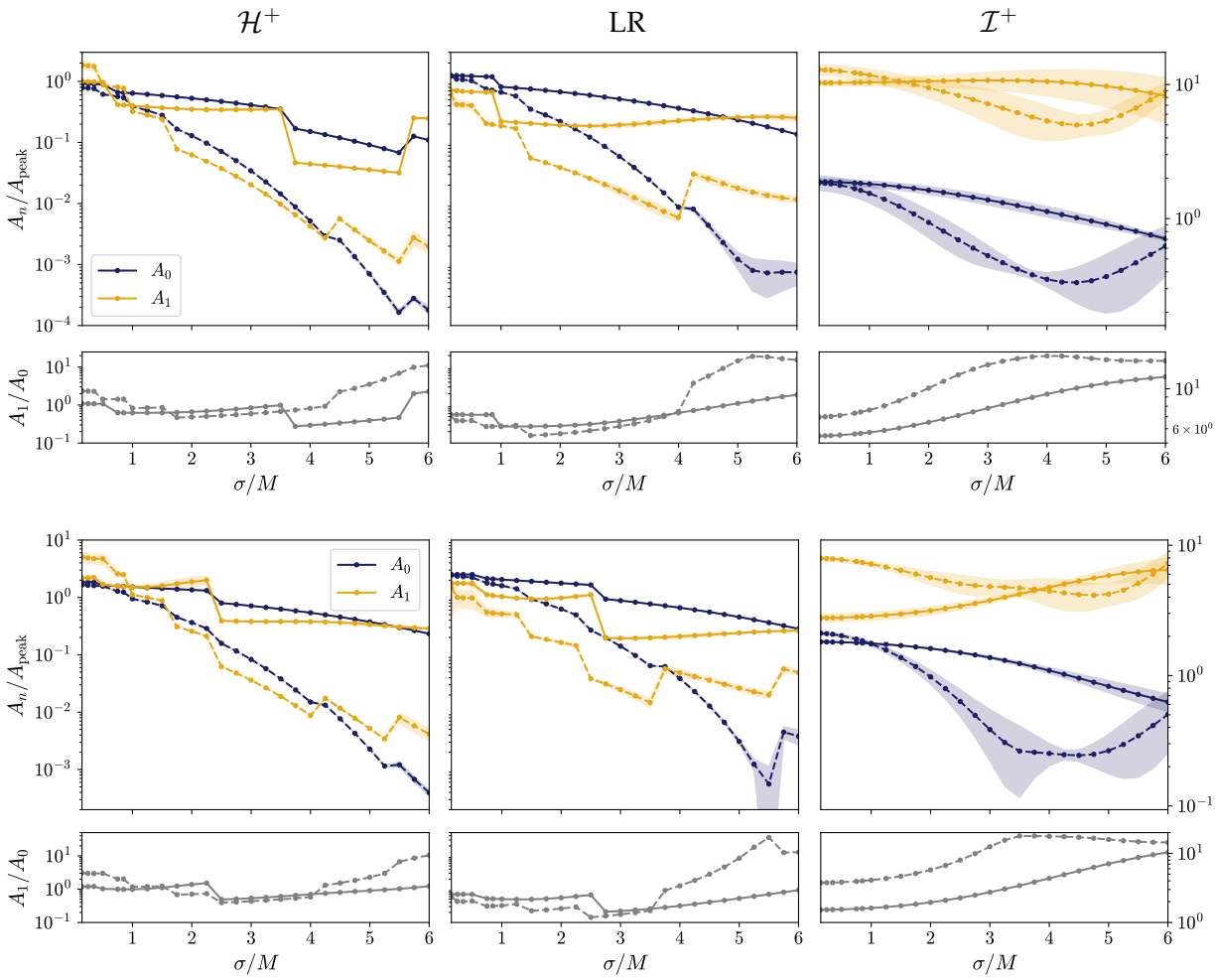

Figure 4.4: Amplitudes of the fundamental mode and the first overtone as a function of σ, obtained from a fit with $N = 2$ to data generated by an initial condition with $x_0 = 30.0M$. The solid (dashed) lines correspond to data with $\ell = 2$ ($\ell = 4$). The top (bottom) row shows the calculation when the initial condition is IC1 (IC2). The lower panels display the ratio between the amplitudes of the first overtone and fundamental mode. Left, centre, and right panels correspond to the amplitudes for signals extracted near the horizon ($\mathcal{H}^+$), light ring (LR), and infinity ($\mathcal{I}^+$). The data points correspond to the average values over a stable window $t_0 \in [t_1, t_2]$, $t_2 < 10M$, and the errorbars correspond to the standard deviation.

as can be seen in Figure 4.3, but we do still include it in the fitting model (equation (3.2)), since it improves the extraction of both the fundamental mode and first overtone.

4.3.2 *Dependence on the width of the pulse*

We now study how the excitation of the fundamental mode and first overtone depends on the width of the Gaussian initial data σ, considering both IC1 and IC2 as initial conditions. Varying σ controls the spectral bandwidth of the perturbations: narrow Gaussians probe a broad range of frequencies, whereas wider Gaussians excite a narrower band. This provides a

clean way of studying how the QNM excitation depends on the frequency content of the initial data.

For each value of σ, we extract the amplitudes of the fundamental mode, A_0, and the first overtone, A_1, from a fit with $N = 2$. We consider both IC1 and IC2 and compare the results for signals extracted at three locations: close to the horizon ($r = 2.099M$), at the light ring ($r = 3.000M$) and at infinity ($r = 125M$). The results are shown in Figure 4.4. In the lower panels we display the ratio A_1/A_0, which quantifies the relative excitation of the overtone with respect to the fundamental mode.

Overall, the behaviour obtained for both sets of initial conditions is broadly similar, indicating that the dependence on σ is controlled by spectral properties rather than on whether the initial data is static or not. The main difference appears in the signals extracted at infinity for $\ell = 2$: for small values of σ, IC2 produces an overtone amplitude roughly one order of magnitude smaller than IC1, while the fundamental mode remains comparable in both cases. As σ increases, A_1 grows for IC2 and approaches the values for IC1, whereas the fundamental mode remains similar in both cases. As for the modes with $\ell = 4$, the behaviour is similar for both initial conditions.

For signals extracted at the horizon, the overtone is comparable to the fundamental mode over most of the range considered in σ, since $A_1/A_0 \sim \mathcal{O}(1)$, as observed in Figure 4.4. However, there is a value of σ above which the amplitude of the overtone exceeds that of the fundamental mode. This transition occurs at $\sigma \approx 5.5M$ for $\ell = 2$ and at $\sigma \approx 4M$ for $\ell = 4$. It is important to note that "dominance" here refers to the ratio A_1/A_0, and does not necessarily imply that the overtone is more excited in absolute terms. In general, we can see how for wider Gaussians the amplitudes of the modes decrease, which matches the expectation that narrower Gaussians excite more overtones, even if the relative excitation increases.

The behaviour at the light ring, in the centre panels of Figure 4.4, closely mirrors that at the horizon, and a similar transition in A_1/A_0 is observed. Both A_0 and A_1 tend to decrease with increasing σ, which is consistent with a reduced spectral overlap with higher overtones. The similarity between the horizon and light-ring extractions suggests that both of these locations probe comparable aspects of the dynamics near the peak of the potential barrier.

The behaviour at infinity, however, is completely different. Over the entire range in σ considered, the overtone amplitude exceeds that of the fundamental mode. For $\ell = 2$, the amplitude of the fundamental mode decreases monotonically with increasing σ, while the overtone remains comparatively stable, leading to a steady increase in the relative excitation A_1/A_0. For $\ell = 4$, both amplitudes decrease until reaching a minimum around $\sigma \approx 4.5M$, and

then increase again for larger widths. This increase, however, is not entirely significant, since for large values of σ the signals become very deformed, as shown in Figure 4.1, due to the early onset of the tail. Therefore, we should only trust the results for $\sigma \leq 4.5M$.

We also analysed the non-normalised amplitudes A_n in order to compare with the predictions in Reference [45]. In that work, it is argued that, for Gaussian initial data of the type IC2 with constant amplitude (independent of σ), the maximal excitation of the mode n occurs when the width satisfies

$$\sigma_{\max} = \frac{1}{\sqrt{|\mathrm{Re}(\omega)|}}, \quad \omega = \omega_n^2, \tag{4.6}$$

where ω_n is the QNM frequency. This predicts that higher overtones achieve maximal excitation at larger σ than the fundamental mode. Our results are consistent with this expectation: the value of σ at which A_1 is maximal is larger than for A_0. This is also related to the discussion in Section 4.2.2, in which it was highlighted that the fundamental mode is maximally excited for some σ_{crit} and exponentially suppressed for $\sigma > \sigma_{\mathrm{crit}}$. The resulted presented here, however, extends to higher overtones.

We conclude that the width of the initial data affects significantly the excitation of QNMs: narrow Gaussian profiles produce a higher absolute excitation of both the fundamental mode and first overtone, while wider profiles suppress the absolute excitation. This can also be understood in terms of the spectral content of the initial data. Given that narrow Gaussian contain a broad Fourier spectrum, they tend to excite many overtones, while wide Gaussians only excite the QNMs for which the real part of the frequency overlaps with the Fourier spectrum. As a result, wide initial data can be interpreted as adiabatic perturbations, which hardly excite QNMs. As for the relative excitation, it increases with σ due to the exponential suppression of the fundamental mode, which was predicted in [75].

4.3.3 *Dependence on the location of the pulse*

We now analyse how the excitation of the fundamental mode and first overtone depends on the location of the initial Gaussian perturbation, x_0. While the previous subsection isolated spectral effects by varying the width σ, here we fix σ and vary the position of the pulse in order to probe how the QNM excitation depends on where the perturbation is initially placed relative to the effective potential and light ring.

To avoid artifacts associated with compact support near the boundaries and to focus on the delta-function limit, we employ narrow Gaussians with $\sigma = 0.5M$. The amplitudes A_0 and A_1 are extracted from fits with $N = 2$ to signals computed for both IC1 and IC2, and for the three

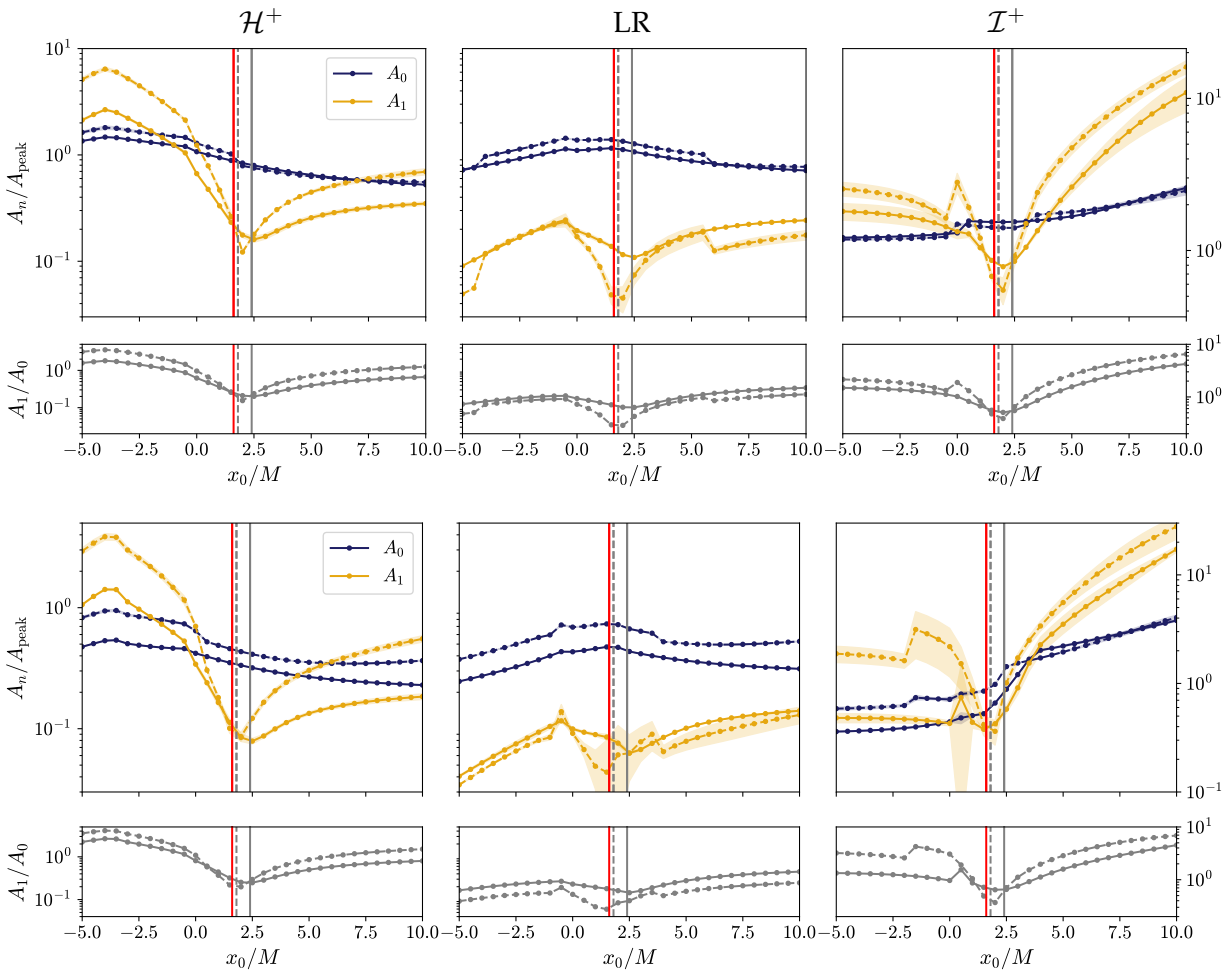

Figure 4.5: Amplitudes of the fundamental mode and the first overtone as a function of x_0, obtained from a fit with $N = 2$ to data generated by an initial condition with $\sigma = 0.5M$. Solid (dashed) lines correspond to data with $\ell = 2$ ($\ell = 4$). The top (bottom) row shows the calculation when the initial condition is IC1 (IC2). The lower panels display the ratio between the amplitudes of the first overtone and fundamental mode. Left, centre, and right panels correspond to the amplitudes for signals extracted near the horizon ($\mathcal{H}^+$), light ring (LR), and infinity ($\mathcal{I}^+$). The data points correspond to the average values over a stable window $t_0 \in [t_1, t_2]$, $t_2 < 10M$, and the errorbars correspond to the standard deviation. The red vertical line marks the light ring; grey lines mark the potential peak for $\ell = 2$ (solid) and $\ell = 4$ (dashed).

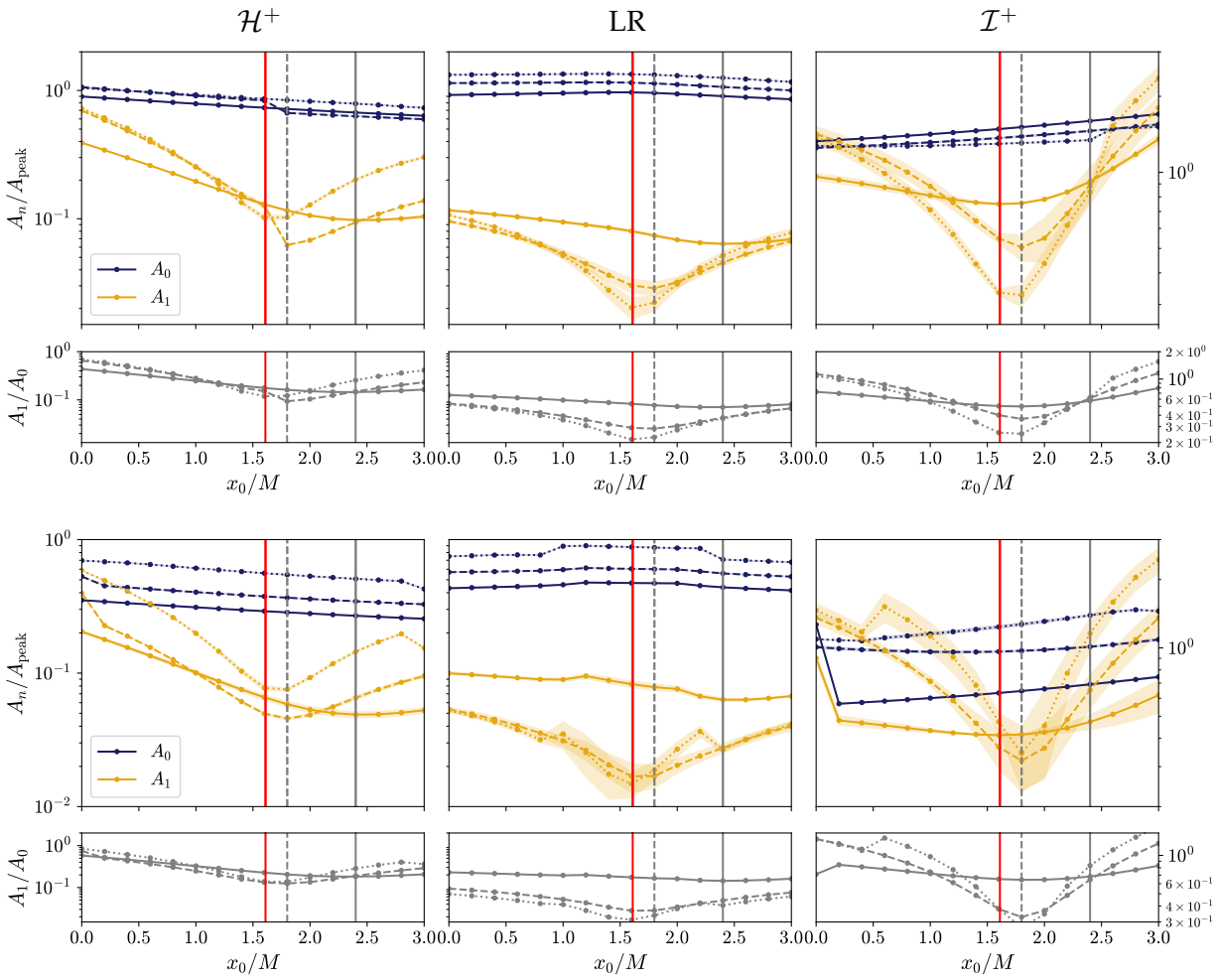

Figure 4.6: Amplitudes of the fundamental mode and the first overtone as a function of $x_0 \in [0, 3M]$ (near the light ring), obtained from a fit with $N = 2$ to data generated by an initial condition with $\sigma = 0.5M$. Solid, dashed, and dotted lines correspond to data with $\ell = 2, 4, 6$, respectively. The top (bottom) row shows the calculation when the initial condition is IC1 (IC2). The lower panels display the ratio between the amplitudes of the first overtone and fundamental mode. Left, centre, and right panels correspond to the amplitudes for signals extracted near the horizon ($\mathcal{H}^+$), light ring (LR), and infinity ($\mathcal{I}^+$). The data points correspond to the average values over a stable window $t_0 \in [t_1, t_2]$, $t_2 < 10M$, and the errorbars correspond to the standard deviation. The red vertical line marks the light ring; grey lines mark the potential peak for $\ell = 2$ (solid) and $\ell = 4$ (dashed).

extraction radii: near the horizon, at the light ring and at infinity. The results are displayed in Figure 4.5. We mark with a red, solid line the location of the light ring, $x_{\rm LR} = 1.61M$, and with grey lines the peaks of the effective potential for $\ell = 2$ (solid) and $\ell = 4$ (dashed), at $x = 2.4M$ and $x = 1.8M$ respectively (see Figure 2.2).

Across all extraction radii and for both initial conditions in Figure 4.5 a common feature emerges: the first overtone is suppressed when the initial pulse is located in the neighbourhood of the light ring. This suppression is particularly evident for signals extracted at the horizon and at infinity. In those cases, the overtone amplitude exceeds that of the fundamental mode over most of the range in x_0, except near the light ring, where the ratio A_1/A_0 decreases sharply. In contrast, for signals extracted at the light ring itself, the overtone is generally suppressed for all x_0, but still exhibits an additional minimum when the initial data is placed near the light ring. This behaviour is the same for the different multipole numbers ℓ.

To further investigate this suppression in the neighbourhood of the light ring, in Figure 4.6 we zoom into the region $x_0 \in [0, 3M]$. We also add to this Figure the amplitudes for a perturbation with $\ell = 6$, represented by a dotted line. The results reveal that the suppression is more precisely correlated with the peak of the corresponding effective potential than with the light ring itself. In particular, for $\ell = 4$ the overtone amplitude reaches a minimum coinciding with the location of the peak of the potential. For $\ell = 2$ the same trend is present but less pronounced, since the overtone amplitude decreases more mildly. This behaviour is reflected in the lower panels, where the ratio A_1/A_0 exhibits a dip near the potential maximum for each multipole.

As the multipole number increases, the location of the peak of the corresponding potential displaces towards the location of the light ring. This is illustrated in Figure 4.6 for $\ell = 6$, where the minimum relative excitation moves closer to the light ring location. Therefore, in the eikonal limit we expect the minimum in the relative excitation to coincide with the location of the light ring.

As shown in Figures 4.5 and 4.6, the amplitude of the overtone is suppressed but it is not zero. This is consistent with the fact that the initial data considered is a Gaussian of finite width rather than a delta distribution.

This suppression of the overtone can be understood in terms of the nodal structure of the QNM radial functions. In [80], an ansatz for the radial function for overtones in the eikonal limit is provided. This radial function has a zero at the light ring of the same order as the overtone number. As explained in Section 2.2, the solution to the wave equation is the convolution of the initial data and the radial function for the QNMs. Therefore, if one considers an initial

condition that only has support in a region in which the radial function for the QNMs vanishes, it is reasonable to expect no excitation of that QNM. This is precisely what our results show. This is also consistent with the fact that, for the data extracted at the light ring, the amplitude of the overtone is suppressed relative to the fundamental mode across the whole range in x_0.

We conclude that the position of the initial perturbation plays a crucial role in QNM excitation. When the pulse is placed near the peak of the effective potential, the first overtone is suppressed relative to the fundamental mode. This suppression is robust across extraction radii, and is related to the geometric structure of the potential barrier. These results reinforce the idea, presented in Section 2.3, that the light ring region and the associated potential peak are central to understanding the excitation of QNMs.

Although these results rely on an idealized situation, in which we have a non-spinning, isolated BH, they allow us to build some intuition for more complex, astrophysically relevant scenarios. The main takeaway from this study is that perturbations placed in the neighbourhood of the light ring do not excite overtones. We can understand it also the other way around: observing overtones in the signal implies that the perturbation does not come from the neighbourhood of the light ring.

5

SOURCE-DRIVEN PROBLEM

In the first part of the thesis, we have focused on investigating the excitation of a Schwarzschild BH by evolving a Gaussian perturbation with the homogeneous RW equation (2.15), thereby probing the linear response of the spacetime to a gravitational perturbation. This approach isolates the BH's dynamical content (prompt response, ringdown, and late-time tail) without any external forcing.

To extend this analysis to a more astrophysically motivated scenario, we now consider the excitation produced by an infalling particle with prescribed velocity v. We focus on trajectories with tunable velocities for two main reasons. First, prescribing the trajectory implies that the particle does not follow a geodesic and therefore acts as an active source of radiation during its motion. This allows us to disentangle and compare the ringdown generated by radiation emitted along the trajectory from that directly associated with the particle crossing the light ring. Second, treating the velocity as a free parameter provides a controlled way of studying how the dynamics of the source itself affect the resulting waveform and the excitation of QNMs. Rather than solving the full gravitational perturbation problem with some energy-momentum tensor, we adopt a simplified model in which a scalar field is sourced by a point-particle moving along a non-geodesic trajectory, approximated numerically by a very narrow Gaussian profile. Although simplified, this scalar toy model provides a controlled setting in which we can study how a localized, dynamical source with tunable velocity excites the characteristic modes of a Schwarzschild BH.

Figure 5.1 shows the trajectories followed by infalling particles for different values of the velocity, which we choose to be of the form $x = x_0 + vt$, with $v < 0$ corresponding to infall. Since the trajectories are parametrized in terms of the tortoise coordinate x, for which the horizon is located at $x \to -\infty$, the particle asymptotically approaches the horizon and therefore never crosses it at a finite coordinate time. Consequently, trajectories do not intersect $\mathcal{H}^+$ in the Penrose diagram, but instead terminate at future timelike infinity i^+.

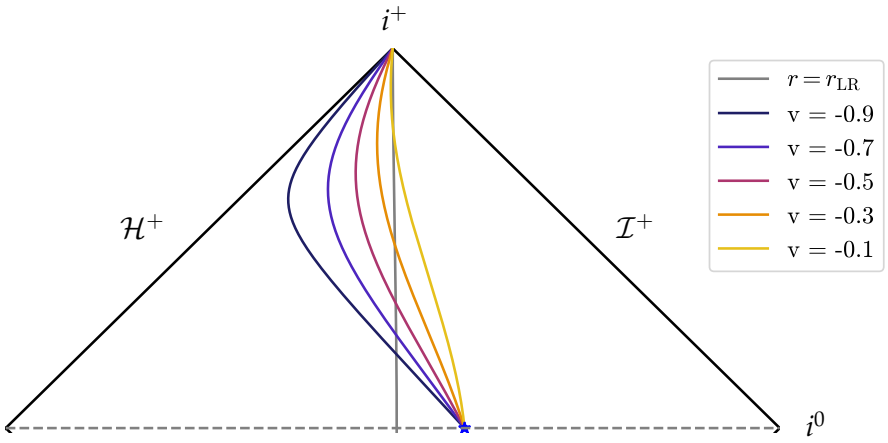

Figure 5.1: Trajectories followed by an infalling particle with velocity v and initial position $x_0 = 30.0M$, represented with a star, on the exterior region of the Penrose diagram of the Schwarzschild BH. The grey line indicates the location of the light ring, whereas the coloured lines mark the trajectory of the corresponding particle.

5.1 FRAMEWORK

Let us consider a scalar field Φ sourced by a point-particle of mass m_p, described by the action [81]

$$S = \frac{-1}{8\pi}\int d^4x\sqrt{-g}g^{\mu\nu}\partial_\mu\Phi\partial_\nu\Phi - m_p\int(1-\Phi)\sqrt{-g_{\mu\nu}\dot{x}_p^\mu\dot{x}_p^\nu}d\tau, \tag{5.1}$$

where $x_p(\tau)$ is the trajectory of the particle and the dot represents differentiation with respect to the proper time of the particle τ. The first term corresponds to the kinetic term of the scalar field, while the second one encodes both the motion of the test particle and its coupling to the scalar field.

The energy momentum tensor associated with the point-particle in (5.1) is [58, 81]

$$T^{\mu\nu}(x) = m_p\int d\tau\,\frac{u^\mu u^\nu}{\sqrt{-g}}\delta^{(4)}(x - x_p(\tau)) \tag{5.2}$$

where $u^\mu = dx_p^\mu/d\tau$ is the 4-velocity of the particle. Varying the action with respect to Φ yields the equation of motion for the scalar field

$$\Box\Phi = -4\pi T, \tag{5.3}$$

where $T = g_{\mu\nu}T^{\mu\nu}$ is the trace of the energy momentum tensor. Using $g_{\mu\nu}u^\mu u^\nu = -1$ this becomes

$$T = \frac{-m_p}{\sqrt{-g}u^t}\delta^{(3)}(\mathbf{x} - \mathbf{x}_p(t)). \tag{5.4}$$

We decompose the scalar field into spherical harmonics as

$$\Phi = \sum_{\ell m} \frac{\psi_{\ell m}}{r} Y_{\ell m}(\theta, \phi), \tag{5.5}$$

where $\psi_{\ell m}$ is the RW function. Substituting this decomposition into equation (5.3) and considering a Schwarzschild background, one obtains a RW-type equation ruling the scalar perturbations [59]

$$\left(\frac{\partial^2}{\partial x^2} - \frac{\partial^2}{\partial t^2} \right) \psi_{\ell m} - V_\ell^{\text{scalar}}(r) \psi_{\ell m} = \mathcal{S}_{\ell m}, \tag{5.6}$$

where $\mathcal{S}_{\ell m} = -4\pi r T$ is the source of the scalar perturbation and

$$V_\ell^{\text{scalar}}(r) = f(r) \left[\frac{\ell(\ell+1)}{r^2} + \frac{2M}{r^3} \right]. \tag{5.7}$$

To extract the multipolar components of the source, we decompose the delta function of equation (5.4) into spherical harmonics

$$\frac{\delta^{(3)}(\mathbf{x} - \mathbf{x}_p(t))}{\sqrt{-g}} = \frac{\delta(r - r_p(t))}{r^2} \sum_{\ell m} Y^*_{\ell m}(\Omega_p) Y_{\ell m}(\Omega) \tag{5.8}$$

which leads to

$$T = \frac{-m_p}{u^t} \cdot \frac{\delta(r - r_p(t))}{r^2} \sum_{\ell m} Y^*_{\ell m}(\Omega_p) Y_{\ell m}(\Omega). \tag{5.9}$$

Projecting onto a given (ℓ, m) mode using orthogonality, we obtain

$$\mathcal{S}_{\ell m} = -4\pi r T = \frac{4\pi m_p Y^*_{\ell m}(\Omega_p)}{u^t} \cdot \frac{\delta(r - r_p(t))}{r}. \tag{5.10}$$

Equation (5.10) provides the exact source term for a radially infalling particle. However, for the purpose of isolating and understanding the ringdown response induced by this particle, we can adopt a simplified description. Following [82], we model the source as

$$\mathcal{S} = f(r) \frac{\delta(x - x_p(t))}{r}, \tag{5.11}$$

where $x_p(t) = x_0 + vt$ is the trajectory followed by the source, with x_0 the initial position and v is the velocity ($v < 0$ for an infalling source), and $r = r(x)$ is a to be understood as function of the tortoise coordinate x. Note that the $f(r)$ factor is a Jacobian term accounting for the coordinate transformation $r \to x$ inside the delta function. This expression captures the essential features of equation (5.10): a localized source moving along a radial trajectory. In particular, the chosen radial scaling reproduces the $1/r$ dependence of the exact multipolar

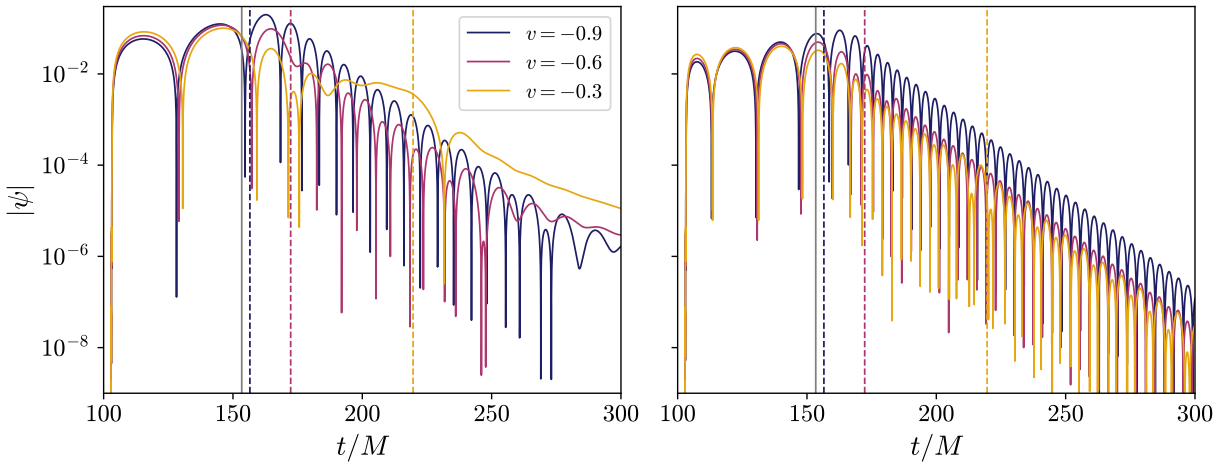

Figure 5.2: Numerical solutions of the sourced scalar perturbation equation (5.6) for a radially infalling particle with different velocities initially placed at $x_0 = 30M$, and extracted at $r = 125M$. On the left (right) panel we plot the signal produced by a perturbation with $\ell = 2$ ($\ell = 4$). The dashed lines correspond to the moment in which the corresponding particle crosses the light ring.

source for a point-particle (up to normalization factors and the redshift term u^t), therefore preserving the dominant radial behaviour while simplifying significantly the dynamics.

For the numerical implementation, we approximate the source (5.11) by a narrow Gaussian profile

$$\mathcal{S} = \frac{f(r)}{r} \frac{1}{\sigma\sqrt{2\pi}} \exp\left[-\frac{(x - x_0 - vt)^2}{2\sigma^2}\right]. \tag{5.12}$$

We set $\sigma = 0.1M$ and $x_0 = 30.0M$ for our simulations.

To solve equation (5.6) we need to impose initial data. If the particle is initially placed at infinity, the initial value data can be taken as zero, so that the spacetime is unperturbed until the gravitational influence of the particle is felt. However, if the particle starts from a finite value, we should specify compatible initial data. For our analysis we consider a toy model, and for the sake of simplicity we take the initial data to be zero. As a consequence, the evolution develops a small burst of spurious early-time radiation ("junk radiation"). In our simulations, this transient appears before the prompt response and has a negligible amplitude, of order 10^{-25}–10^{-20}. Given that the amplitude of the junk radiation is around 10 orders of magnitude smaller than the ringdown signal, it does not affect the subsequent physical signal. Since our goal is to study a simplified model, we adopt trivial initial data throughout.

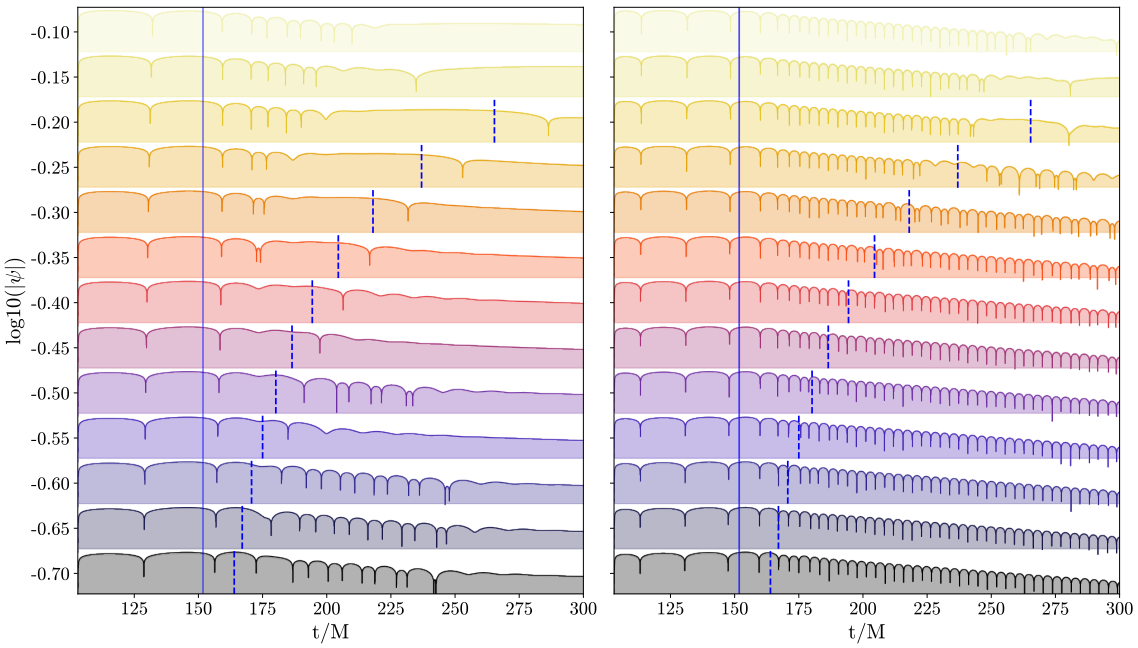

Figure 5.3: Numerical solutions of the sourced scalar perturbation (5.6) for a radially infalling particle with different velocities (rows) initially placed at $x_0 = 30M$, extracted at $r = 125M$ for a perturbation with $\ell = 2$ ($\ell = 4$) on the left (right) panel. The vertical, dashed line marks the instant of time in which the particle crosses the light ring, whereas the solid line marks the corresponding crossing time for a particle moving at the speed of light.

5.2 NUMERICAL SOLUTIONS FOR THE SOURCED PROBLEM

Selected numerical solutions of equation (5.6) are shown in Figure 5.2 for different values of the velocity v. The left (right) panel shows solutions obtained for perturbations with $\ell = 2$ ($\ell = 4$). The vertical dashed lines mark the instant at which the corresponding particle crosses the light ring, computed as

$$t_{\rm cross} = \frac{x_0 - x_{\rm LR}}{|v|} + x_{\rm obs} - x_{\rm LR} = \frac{30M–1.61M}{|v|} + 125M - 1.61M, \tag{5.13}$$

where x_0 is the initial position of the particle, $x_{\rm LR}$ is the location of the light ring, and $x_{\rm obs} = 125M$ is the extraction radius.

The structure of the signal depends on whether the particle has crossed the light ring before the radiation reaches the observer. For $|v| \geq v_{\rm crit} \simeq 0.73$ the particle crosses the light ring before any radiation arrives at the observing point $x_{\rm obs}$, producing signals structurally identical to those in Figure 4.1. For $|v| < v_{\rm crit}$, however, the signals contain two distinct windows in which we can observe ringdown, which are more clearly resolved in Figure 5.3.

The first window precedes the light ring crossing and is sourced by radiation produced as the particle travels towards the potential barrier. This radiation scatters off the potential and

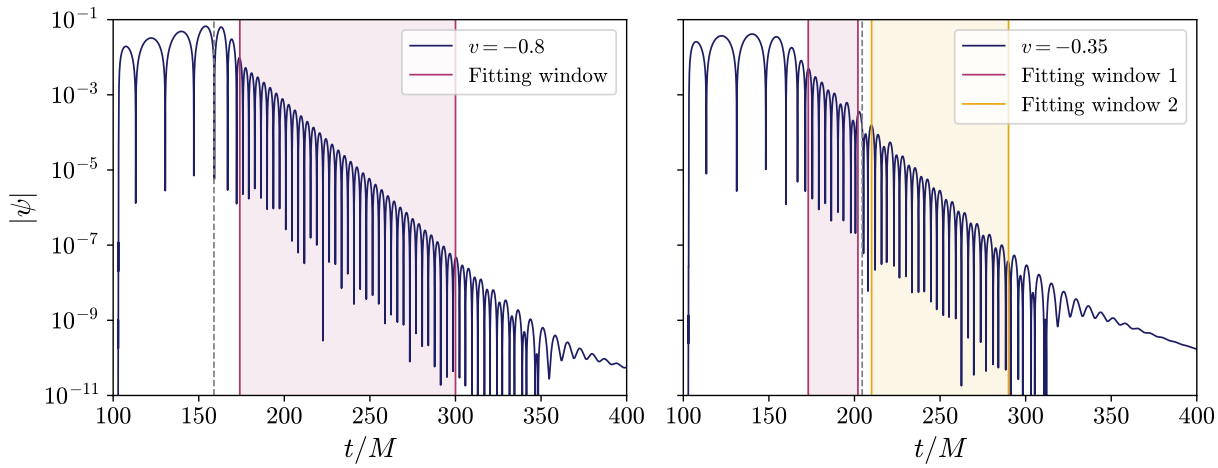

Figure 5.4: Ringdown signals generated by an infalling particle with velocity $v = -0.8$ (left) and $v = -0.35$ (right) and initial position $x_0 = 30M$, for a perturbation with $\ell = 4$. The grey, dashed line marks the instant in which the particle crosses the light ring. The shadowed areas mark the windows in which we fit to QNMs.

generates a ringdown quantitatively similar to those studied in Section 4. The second window is triggered by the particle crossing the light ring itself. For $\ell = 2$, the QNMs are weakly excited in this second window, leaving mainly the late-time power-tail; for $\ell = 4$ the mode excitation is more pronounced, as visible for $v = -0.3$ in Figure 5.2. Whether the mode content in fact differs between the two ringdown windows is examined in Section 5.3.

Focusing on the low velocity regime, $|v| < 0.3$, Figure 5.3 shows that both ringdown windows are clearly present, but that the mode excitation in the second window diminishes as $|v|$ decreases. At sufficiently low velocities the particle crosses the light ring quasi-adiabatically, so the perturbation it induces is too smooth to excite QNMs appreciably. The second window then consists almost entirely of the tail, with the signal dominated instead by the radiation emitted during the infall phase. However, a more detailed analysis should be carried out in order to determine its exact origin and properties.

As the velocity $|v|$ decreases, an unexpected feature between the tail coming from the first ringdown and the light ring crossing appears: a series of low-frequency oscillations that modulate the tail of this first window. These oscillations are consistent with an interference pattern between the decaying tail of the first ringdown and the radiation continuously emitted by the still-infalling particle.

	ωM	
n	$\ell = 2$	$\ell = 4$
0	0.48364 - 0.09675i	0.86741 - 0.09639i
1	0.46385 - 0.29560i	0.85580 - 0.29087i
2	0.43054 - 0.50855i	0.83369 - 0.49032i

Table 5.1: Frequencies for the fundamental mode and the first two overtones for a scalar perturbation, tabulated in [72]. Accurate to the decimal digits shown.

n	ωM	$\delta\omega_{\mathrm{R}}/\omega_{\mathrm{R}}(\%)$	$\delta\omega_{\mathrm{I}}/\omega_{\mathrm{I}}(\%)$
0	0.86779 - 0.09644i	0.04	0.05
1	0.80562 - 0.25760i	5.86	11.84

Table 5.2: Frequencies of the fundamental mode and first overtone, extracted from the signals generated by an infalling particle with $v = -0.8$ (second column). The third and fourth column correspond to the relative errors with respect to the tabulated frequencies in 5.1.

5.3 MODE CONTENT

For signals exhibiting two distinct ringdown windows, we investigate whether the mode content differs between the window driven by scattered radiation and that driven by the particle crossing the light ring. As discussed above, this analysis is cleanest for $\ell = 4$, where both windows are well resolved.

We begin analysing a signal that has only one ringdown window, so that the modes are excited solely by the infalling particle. Specifically, we analyse the signal generated by a particle with $v = -0.8$, shown in the left panel of Figure 5.4, fitting QNMs over the window $t \in [174M, 300M]$. We apply the MPM, (Section 3.3, Appendix A) with two models: one in which the frequencies are free parameters, and one in which they are fixed to the tabulated values of Table 5.1 [72]. The results of these fits are shown in Figure C.1 of Appendix C, and the extracted frequencies, for the model with free frequencies, are gathered in the second column of Table 5.2.

Both models reproduce the signal well. Examining the residuals, the free-frequency fit performs better at earlier times, where overtones are still present and allowing the frequencies to vary captures their contribution more accurately. At later times, once the overtones have decayed, fixing the frequencies yields a tighter fit: the fundamental mode is recovered to within 0.05% of the tabulated value, while the first overtone carries relative errors of $\sim 6\%$ in the real part and $\sim 12\%$ in the imaginary part, consistent with the well-known difficulty of resolving overtones at late times.

n	ωM (window 1)	$\delta\omega_R/\omega_R(\%)$	$\delta\omega_I/\omega_I(\%)$	ωM (window 2)	$\delta\omega_R/\omega_R(\%)$	$\delta\omega_I/\omega_I(\%)$
0	0.86727 - 0.09647i	0.01	0.08	0.86627 - 0.09569i	0.13	0.73
1	0.83665 - 0.29486i	2.24	1.42	0.31988 - 0.23163i	62.62	21.09

Table 5.3: Frequencies of the fundamental mode and first overtone, extracted from the signals generated by an infalling particle with $v = -0.35$, together with the relative errors (%) with respect to the values tabulated in Table 5.1.

We now turn to a signal with two ringdown windows, produced by a particle with $v = -0.35$ and shown in the right panel of Figure 5.4. We fit both windows independently using the same two models, fixed and free frequencies, with results shown in Figure C.2 of Appendix C.

In the first window, the fundamental mode is again recovered with sub-percent accuracy, and the first overtone to within $\sim 2\%$ in both parts. The second window, however, exhibits a different behaviour. Although the fundamental mode is still recovered with an accuracy better than 1%, the real part of the first overtone frequency deviated by more than 60% from the expected QNM value. This strongly suggests that the second window does not correspond to a clean excitation of the first overtone of the QNM spectrum.

To further investigate the origin of this artifact, we analysed the stability of the extracted contribution across different fitting windows and found that it does not exhibit the approximate stability expected for a QNM. This indicates that the observed feature should not be interpreted as a true overtone excitation, but rather as an artifact arising from the structure of the signal itself. A plausible explanation is that it originated from the interference between the second ringdown signal and the prompt response generated by the source. A more detailed analysis would nevertheless be required to fully determine its physical origin.

This contrast between the two windows suggests that the radiation- and particle-driven ringdowns differ not only in amplitude but in their overtone structure and overall spectral structure.

5.4 EFFECT OF THE SOURCE ON THE SIGNALS

We investigate how the signal observed at infinity is affected when the source is switched off at a given tortoise coordinate position x_{off}. This models the scenario in which the particle disappears at that position. To this end, we replace the source in equation (5.11) by

$$\mathcal{S}^{\text{off}}_{\ell m} = f(r)\frac{\delta(x - x_0 + vt)}{r}\frac{1}{1 + e^{-a(x - x_{\text{off}})}}, \tag{5.14}$$

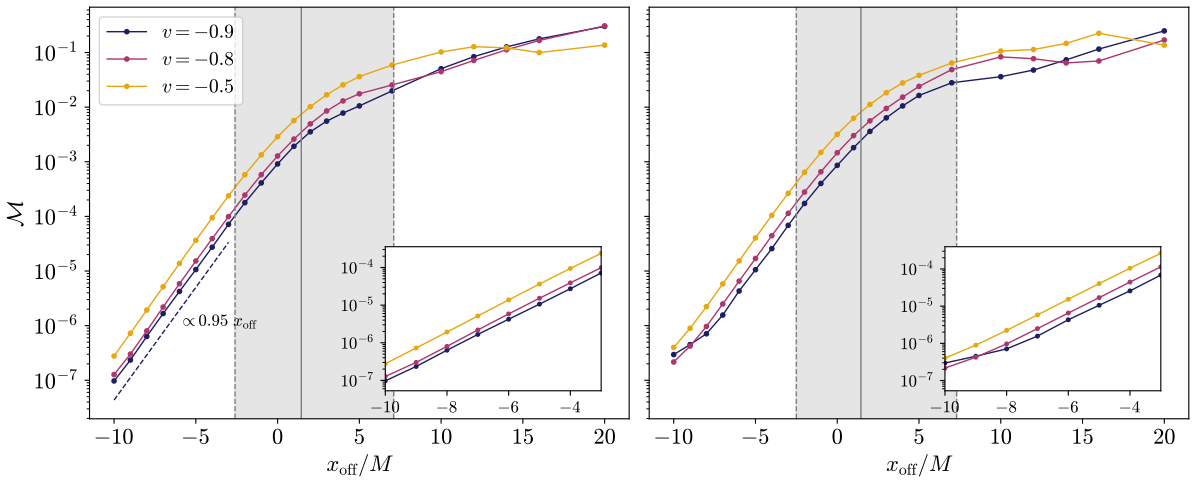

Figure 5.5: Mismatch between the signal computed with the source present through the whole evolution and the signal in which the source is turned off at a position $x_{\rm off}$, for particles with $v \in \{-0.9, -0.8, -0.5\}$ initially placed at $x_0 = 30M$. The signals on the left (right) panel correspond to perturbations with $\ell = 2$ ($\ell = 4$). The solid, grey line marks the position of the light ring, and the shaded region corresponds to the FWHM of the scalar potential. The inset plot shows the mismatch for signals in which the source is turned off after crossing the potential barrier.

where the coefficient $a = 0.01M^{-1}$, so that the suppression is spatially sharp compared to the width of the potential barrier. The smoothing factor that we have added extinguishes the source for $x < x_{\rm off}$, therefore keeping the source for $x > x_{\rm off}$ and killing it inside. For the numerical implementation, we carry out an approximation of the delta-function analogous to the one in equation (5.12). For each velocity v and each value of $x_{\rm off}$, we solve equation (5.6) and compute the mismatch (3.3) between this signal and the reference signal in which the source is active throughout the entire infall. The mismatch therefore quantifies how much the waveform observed at infinity changes when the source is removed at $x_{\rm off}$.

Figure 5.5 shows the results for perturbations with $\ell = 2, 4$ on the left and right panels, respectively, for particles with $v \in \{-0.9, -0.8, -0.5\}$ and initial position $x_0 = 30M$. When the source is switched off outside the potential barrier (right of the shaded FWHM region of the potential), the mismatch is large, $\mathcal{M} \gtrsim 10^{-2}$. Inside the barrier but near its peak the mismatch falls steeply, and for $x_{\rm off}$ well inside the barrier it decays exponentially with the same rate for all three velocities and both multipole numbers, reaching $\mathcal{M} \sim 10^{-4}$ at the light ring and dropping further afterwards.

The exponential suppression has a straightforward physical interpretation: the radiation generated inside the potential barrier and directed outwards is predominantly reflected back, so it never reaches the far-field observer. More precisely, the barrier acts as a frequency-dependent filter: for frequencies below the scale set by the peak of the potential, roughly $\omega \leq \omega_{n=0}$, the transmission coefficient is essentially zero [53], so any radiation inside the barrier is strongly

attenuated before reaching infinity. Consequently, once the particle has passed through the barrier, removing it from the simulation produces a negligible change in the signal at infinity. This has a practical implication for computationally expensive simulations, since it points towards the fact that the source can be safely switched off after the particle crosses the light ring, substantially reducing the integration time without meaningful loss of accuracy in the extracted signal.

6

CONCLUSIONS AND FUTURE PROSPECTS

Understanding how QNMs are excited is essential for connecting BH perturbation theory with GW observations, and is one of the central open questions in BH spectroscopy. While the QNM spectrum itself is known to high precision, the mechanisms controlling mode excitation remain comparatively poorly understood. In this thesis, we aim to contribute to this problem. In particular, we investigate how the properties of the perturbation determine the amplitude of the excited modes and whether the excitation process can be regarded as localized in spacetime.

We begin by reviewing the fundamental aspects of BH perturbation theory, focusing on gravitational perturbations of a Schwarzschild background, the description of the ringdown as a superposition of QNMs, and the relation between QNMs and the light ring. Within this framework, we generate ringdown signals by numerically solving the homogeneous perturbation equation using Gaussian initial data. We consider both static and non-static sets of Gaussian initial data (see equations (4.1) and (4.2)) and analysed how the parameters characterizing the initial perturbation, namely its width σ and initial position x_0, affect the resulting ringdown signals.

Overall, we observe that both sets of initial data exhibit similar behaviour with respect to their dependence on σ and x_0. This strongly suggests that QNM excitation is governed primarily by the spectral properties of the perturbation rather than by whether the initial data is static or dynamical. Before analysing the dependence on the Gaussian parameters themselves, we first study the impact of the fitting window on the extraction of the QNM amplitudes. We observe that the extracted amplitudes of the QNMs remain approximately stable over a finite range of fitting windows (Figure 4.3), consistent with the exponentially damped nature of QNMs: attempting to extract amplitudes of overtones after they have decayed leads to unstable results. These observations allow us to identify appropriate fitting intervals and to define QNM amplitudes as average values over the corresponding stability windows.

Regarding the dependence on the width, we find that the amplitudes extracted from signals observed close to the horizon and at the light ring display remarkably similar behaviour (Figure 4.4), suggesting that these extraction regions probe similar aspects of the dynamics near the peak of the potential. In both cases, we observe that the amplitudes for the fundamental mode and first overtone remain of the same order of magnitude. By contrast, the behaviour of the amplitudes corresponding to signals extracted at infinity differs substantially. In this case, for all widths considered, the overtone amplitude exceeds that of the fundamental mode. Moreover, we find that the relative excitation of the overtone with respect to the fundamental mode increases with increasing σ. This behaviour is consistent with the fact that the excitation of the fundamental mode is exponentially suppressed for large values of σ, as already mentioned in Reference [75]. This can be physically interpreted in terms of wide initial data corresponding to more adiabatic perturbations, which tend to excite less QNMs due to their spectral content.

When studying the dependence on the initial location position of the perturbation, we consider a narrow Gaussian pulse ($\sigma = 0.5M$), with the goal of approaching the delta-function limit. In this case, a common feature emerges across all extraction radii (Figures 4.5 and 4.6): the suppression of the first overtone relative to the fundamental mode when the pulse is located in the neighbourhood of the light ring. We find that the minima in the relative excitation match the position of the peak of the RW potential rather than the exact location of the light ring. In the eikonal limit, however, these two locations coincide, and the minimum is attained precisely at the light ring. This result is closely related to the property that, in the eikonal limit, the radial functions of the overtones possess zeroes at the light ring, with the order of the zero matching the overtone number [80]. Consequently, if the perturbation is sufficiently localized in a region where the radial function of a given overtone vanishes, the extraction of that mode is expected to be strongly suppressed. These results therefore demonstrate that the spatial location of the perturbation plays a crucial role in QNM excitation. In particular, they suggest that the observation of overtones in a ringdown signal indicates that the perturbation cannot be localized exclusively in the neighbourhood of the light ring.

After analysing the homogeneous problem, in which we have studied the linear response of the spacetime to a gravitational perturbation, we turn to the source-driven case as a more astrophysically motivated scenario. Rather than considering the full gravitational perturbation problem, we adopt a simplified scalar toy model in which the perturbation is sourced by a point-particle moving along a non-geodesic trajectory, which we approximate as a narrow Gaussian profile with $\sigma = 0.1M$. This setup serves as a controlled framework for studying QNM excitation produced by a localized, dynamical source with tunable velocity.

The structure of the signal obtained numerically depends on whether the particle crosses the light ring before or after the radiation reaches the observer (Figures 5.2 and 5.3). If the particle crosses the light ring before any radiation arrives at the observation point, the signal exhibits a single ringdown phase, similar to the ones corresponding to the homogeneous problem, induced by the particle crossing the light ring. By contrast, if the particle crosses the light ring after some of the radiation has already reached the observer, two ringdown windows are observed in the signal. The first window is sourced by the radiation produced as the particle moves towards the light ring, which gets scattered by the potential. The second window is triggered by the particle crossing the light ring itself. We analyse the mode content in both regimes, and found evidence that the radiation- and particle-driven ringdowns differ not only in amplitude, but also in their overtone structure.

Finally, we investigate the effect of the source on the signals, in particular how the signal changes when the source is artificially turned off at a given position $x_{\rm off}$ (Figure 3.3). To quantify the change in the signal observed at infinity, we compute the mismatch between the signal in which the source is turned off and the reference signal in which the source is active through the entire infall. For perturbations with $\ell = 2, 4$, we find that the mismatch decreases exponentially once the source is switched off after crossing the potential barrier. This behaviour can be physically understood from the fact that radiation generated inside the barrier and directed outwards is predominantly reflected back by the potential, preventing it from reaching far-field observers. From a practical perspective, this result has important implications for computationally expensive simulations, as it shows that the source can be safely removed once it crosses the light ring without significantly affecting the waveform extracted at infinity, thereby substantially reducing the computational cost of the evolution.

On the whole, the results presented in this thesis indicate that QNM excitation is controlled not only by the geometry of spacetime, but also by detailed properties of the perturbation, including its spectral content, localization, and dynamical origin. The results show that the light ring alone does not determine the complete ringdown response, and that the excitation of overtones is highly sensitive to where and how the perturbation is generated. These findings further reinforce the view that the ringdown signal encodes a richer dynamical structure than what is captured by purely geometric arguments.

Although the simplified setups considered in this thesis have allowed to isolate and investigate specific aspects of QNM excitation, they also highlight the need to extend this analysis to more realistic scenarios. The most immediate direction is the generalization of these results to Kerr spacetime, where rotation introduces new features in both the QNM spectrum and the

structure of the effective potential, which is necessary given than most of the BHs we observe rotate. In the context of the source-driven model studied here, several open questions remain, particularly regarding the interference between the two ringdown windows observed at low particle velocities. Understanding this interference can be extremely useful to gain further insight into the transition between prompt response, ringdown, and late-time dynamics, which is an active field of research. It is also important to investigate whether the localization and excitation properties identified here persist in full gravitational, source-driven perturbations and in numerical relativity (NR) waveforms. In this direction, analyses similar to the one carried in this thesis could be carried out using NR simulations to study how QNM excitation depends on the parameters of the progenitor binary, including the mass ratio, component spins, eccentricity, and other orbital parameters. From the numerical perspective, the development of more robust fitting procedures capable of reliably extracting a larger number of overtones would be especially valuable, as it would allow the extension of the present analysis to higher-order modes and provide a more complete characterization of the excitation process.

As discussed throughout this thesis, understanding the interplay between the geometry of the spacetime and the properties of the perturbation is essential for developing a complete picture of QNM excitation. Beyond its fundamental theoretical interest, this problem also has direct implications for GW data analysis, since a better understanding of how and under which conditions QNMs are excited can help improve both waveform models and ringdown fitting methods used in observations. This, in turn, is crucial for extracting the maximum amount of physical information from GW signals and for fully exploiting the potential of BH spectroscopy as a probe of strong-field gravity. As detector sensitivities continue to improve and increasingly precise measurements of the ringdown become available, clarifying the mechanisms governing QNM excitation will become progressively more important for interpreting future observations and testing the nature of BHs with high precision.

A

THE MATRIX PENCIL METHOD

The Matrix Pencil Method (MPM) is a parametric spectral estimation technique used to determine the poles $\{z_k\}$ of a given signal [73, 83, 84]. It is known for its high accuracy, robustness, and stability in the presence of noise, which is achieved by recasting the problem in terms of a generalised eigenvalue problem, allowing for systematic rank truncation via singular value decomposition (SVD).

During the ringdown phase, the signal is modelled as a superposition of QNMs, as shown in equation (2.31) and discussed in Section 2.2. Sampling the signal at uniform interval Δt, one can write the discrete time series

$$x[n] = \sum_{k=1}^{K} A_k z_k^n, \quad z_k = e^{-i\omega_k \Delta t}. \tag{A.1}$$

Therefore, the problem of computing the QNM frequencies ω_k reduces to estimating the poles z_k of the sum of complex exponentials.

Let N be the number of data points and L the pencil parameter, such that $K < L < N - K$. The method begins by constructing two $(N - L) \times L$ Hankel matrices from the data points of the time series $x[n]$ as

$$Y_0 = \begin{pmatrix} x[0] & x[1] & ... & x[L-1] \\ x[1] & x[2] & ... & x[L] \\ \vdots & \vdots & \ddots & \vdots \\ x[N-L-1] & x[N-L] & ... & x[N-2] \end{pmatrix} \tag{A.2}$$

and

$$Y_1 = \begin{pmatrix} x[1] & x[2] & ... & x[L] \\ x[2] & x[3] & ... & x[L+1] \\ \vdots & \vdots & \ddots & \vdots \\ x[N-L] & x[N-L+1] & ... & x[N-1] \end{pmatrix}. \tag{A.3}$$

These matrices encode time-shifted embeddings of the data. If the signal contains exactly K exponentials (i.e. it is the number of modes, including the fundamental one, to which we are fitting), the Hankel matrices Y_0 and Y_1 can be factorised as

$$Y_0 = UHV^T \quad \text{and} \quad Y_1 = UHZV^T, \tag{A.4}$$

where the superscript T denotes the transposed. U, V are Vandermonde matrices containing the poles $\{z_k\}$ of the signal,

$$U = \begin{pmatrix} 1 & 1 & ... & 1 \\ z_1 & z_2 & ... & z_p \\ \vdots & \vdots & \ddots & \vdots \\ z_1^{N-L-1} & z_2^{N-L-1} & ... & z_p^{N-L-1} \end{pmatrix}, \quad V = \begin{pmatrix} 1 & 1 & ... & 1 \\ z_1 & z_2 & ... & z_p \\ \vdots & \vdots & \ddots & \vdots \\ z_1^{L-1} & z_2^{L-1} & ... & z_p^{L-1} \end{pmatrix}, \tag{A.5}$$

and H and Z are diagonal matrices containing respectively the amplitudes and the poles from equation (A.1)

$$H = \text{diag}(A_1, A_2, ..., A_p), \tag{A.6}$$

$$Z = \text{diag}(z_1, z_2, ..., z_p). \tag{A.7}$$

This factorisation implies $Y_1 = Y_0 Z$ in the signal subspace.

Consider now the matrix pencil $Y_1 - zY_0$. Using the factorisation above, it can be written as

$$Y_1 - zY_0 = UH(Z - zI_p)V^T. \tag{A.8}$$

If $z \neq z_i$, the matrix $Z - zI_p$ is of rank p. Nevertheless, if $z = z_i$ the rank becomes $p - 1$. Therefore, the poles of the signal reduce the rank of the matrix pencil for $p \leq L \leq N - p$. In other words, the poles z_i are the generalised eigenvalues of (Y_1, Y_0) in the sense that

$$(Y_1 - zY_0)\mathrm{v} = 0 \tag{A.9}$$

for v and eigenvector of the matrix pencil $Y_1 - zY_0$. Equivalently, the non-zero eigenvalues of $Y_0^+ Y_1$ coincide with the poles z_k. The $+$ denotes the Penrose-Moore pseudo-inverse [85].

In realistic ringdown data, the signal can be contaminated by some noise. Consequently, Y_0 and Y_1 are full rank. In order to isolate the signal subspace, one performs the singular value decomposition $Y_0 = U\Sigma V^\dagger$. If the data are well described by K modes, the singular values exhibit a sharp drop after the $K-$th component. Truncating to rank K yields a reduced

representation $Y_0 \approx U_K \Sigma_K V_k^\dagger$. Projecting the pencil onto this $K-$dimensional signal subspace leads to the reduced eigenvalue problem

$$\left(U_K^\dagger Y_1 V_K \Sigma_K^{-1}\right) \mathrm{v} = z\mathrm{v}. \tag{A.10}$$

The resulting eigenvalues z_k provide stable estimates of the physical poles, and thus the QNM frequencies. This is the key to the numerical stability of the MPM.

Once the set of poles $\{z_k\}$ is known (either extracted or fixed a priori), the complex amplitudes $\{A_k\}$ follow from a linear inversion of the full data set [86]. We obtain an overdetermined system of linear equations

$$\begin{pmatrix} z_1^0 & z_2^0 & \dots & z_p^0 \\ z_1^1 & z_2^1 & \dots & z_p^1 \\ \vdots & \vdots & \ddots & \vdots \\ z_1^{N-1} & z_2^{N-1} & \dots & z_p^{N-1} \end{pmatrix} \begin{pmatrix} A_1 \\ A_2 \\ \vdots \\ A_p \end{pmatrix} = \begin{pmatrix} x[0] \\ x[1] \\ \vdots \\ x[N-1] \end{pmatrix}. \tag{A.11}$$

This overdetermined Vandermonde system can be solved using SVD-based pseudoinverse to compute the amplitudes, yielding the least-squares optimal amplitudes for the selected data segment.

B

APPROXIMATING THE TAIL BY EXPONENTIALS

As discussed in Section 4.2.3, the perturbation of a Schwarzschild background at late times exhibits a power-law behaviour of the form

$$\Phi(t) \sim t^{-p}, \quad p = 2\ell + 3, \tag{B.1}$$

commonly referred to as the late-time or Price tail [76]. While this behaviour is intrinsically non-exponential, it can be approximated over finite time intervals as a superposition of purely damped exponentials [79],

$$f(t) = t^{-p} \to f(t) \approx \sum_{n=1}^{N} A'_n e^{-t/\tau_n}, \tag{B.2}$$

with appropriately chosen amplitudes A'_n and decay timescales τ_n. The key idea is that each exponential provides a good approximation to the power-law over a limited range of timescales, so that by the combination of several such exponentials one can reproduce the power-law behaviour over multiple decades in time. In this sense, a late-time tail can be viewed as arising from a continuum (or dense discrete set) of purely damped modes, each characterized by a decay rate but no oscillatory component.

From this perspective, the tail is not fundamentally different from the QNM contribution, but can instead be viewed as the limiting case of modes with vanishing real part and continuous distribution of decay rates. This interpretation also clarifies why the late-time tail can interfere with the QNM signal. In particular, a typical signal in the intermediate regime between QNMs and tail can be approximated, using (B.2) and (2.31), as

$$\psi(t) \sim \sum_n A_n e^{-i\omega_n t} + \sum_k A'_k e^{-t/\tau_k}, \tag{B.3}$$

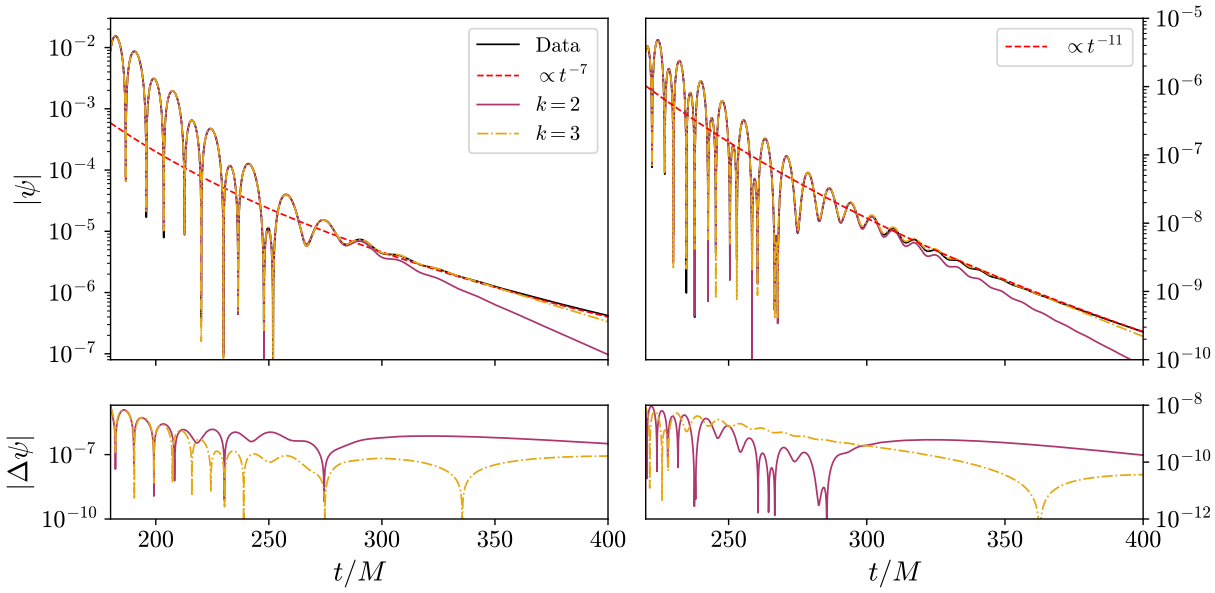

Figure B.1: Fit of the intermediate regime between QNMs and late-time tail for perturbations with $\ell = 2$ (left) and $\ell = 4$ (right) including $k = 2$ and $k = 3$ purely damped exponentials, together with the relevant QNM contributions. The lower panels show the residuals between each fit and the data. The Price law for the tail is plotted with a red dashed line for each multipole number.

where the first sum corresponds to the QNM contribution and the second approximates the tail. Since both terms contain damped exponentials with different decay rates, there exists a time interval in which the QNMs have not yet fully decayed and the tail contribution has already become non negligible. The interference between these oscillatory and non-oscillatory terms leads to amplitude modulations in the signal, which manifest as the beating patterns observed in Figure 4.1.

To illustrate these ideas, we perform fits to signals exhibiting beating patterns in the intermediate regime between the QNM-dominated phase and the late-time tail, for perturbations with $\ell = 2, 4$. In particular, we consider signals generated by initial data of the form IC1 with $x_0 = 30.0M$ and $\sigma = 4.0M$. The results are shown in Figure B.1, where we display fits using $k = 2, 3$ purely damped exponentials in equation (B.3), together with the corresponding residuals in the lower panels. In constructing these fits, we include the dominant QNM contributions alongside the purely damped modes. For $\ell = 2$ both the fundamental mode and first overtone are included, whereas for $\ell = 4$ only the fundamental mode is retained. This difference reflects the earlier onset of the tail for $\ell = 2$, which allows the first overtone to remain relevant within the fitting window. In contrast, for $\ell = 4$ the overtone has already decayed by the time the tail contribution becomes significant and therefore does not contribute to the signal in the interval considered.

For both multipole numbers, the fit including $k = 3$ purely damped exponentials provides a noticeably better description of the signal, particularly in the transition towards the late-time regime, being the residual around one order of magnitude smaller than for the fit with $k = 2$. This improvement is consistent with the interpretation of the tail arising from a dense set of purely damped modes: increasing k allows for a more accurate reconstruction of the underlying power-law behaviour over a finite interval. The residuals further confirm that the inclusion of additional exponential terms systematically reduces the discrepancy between the fit and the data, especially at late times where the tail contribution becomes dominant.

Moreover, these fits make explicit the origin of the beating patterns observed in the signals. In the intermediate regime, the signal is well described by a superposition of QNMs and non-oscillatory contributions, the purely damped components approximating the tail. The interference between these terms produces amplitude modulations, which manifest as the observed beating pattern. This provides direct numerical support for the interpretation of the tail as an effective sum of exponentials and clarifies how its coexistence with QNMs shapes the structure of the signal.

This framework also clarifies why these patterns are more prominent for certain initial data. In particular, wide initial profiles are dominated by low-frequency components, which hardly excite QNMs and enhance the branch cut contribution. Consequently, the tail becomes more relevant at earlier times, so that the overlap between QNMs and the tail increases and the interference becomes more pronounced. In the extreme case in which the QNM excitation is strongly suppressed, the signal can be almost entirely described by the effective sum of exponentials approximating the tail, with no visible ringing.

C

FITS FOR INFALLING PARTICLE

In this Appendix we show the results for the fits discussed in Section 5.3 for both of the signals in Figure 5.4.

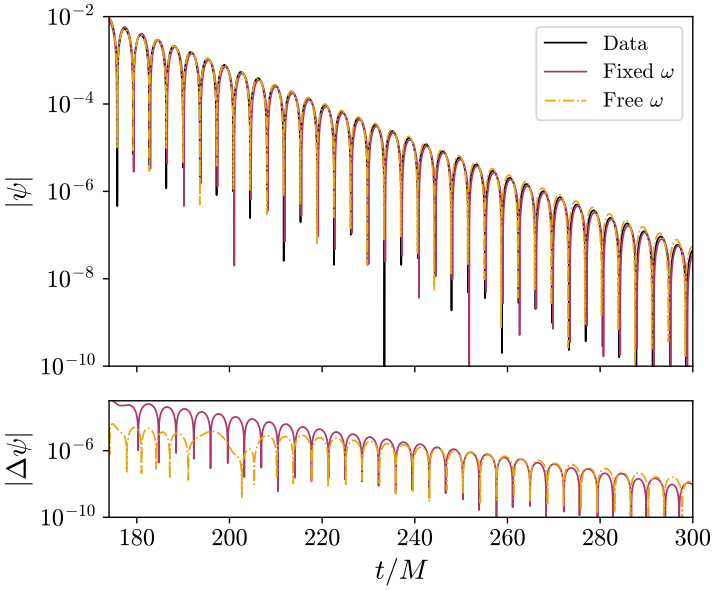

Figure C.1: Fits including 3 modes (fundamental mode and two overtones) for the signal shown in the left panel, for the fitting window in the left panel of Figure 5.4. We show the fit obtained with fixed frequencies (pink) and the one obtained for free frequencies (orange). The lower panel shows the difference between the fits and the data.

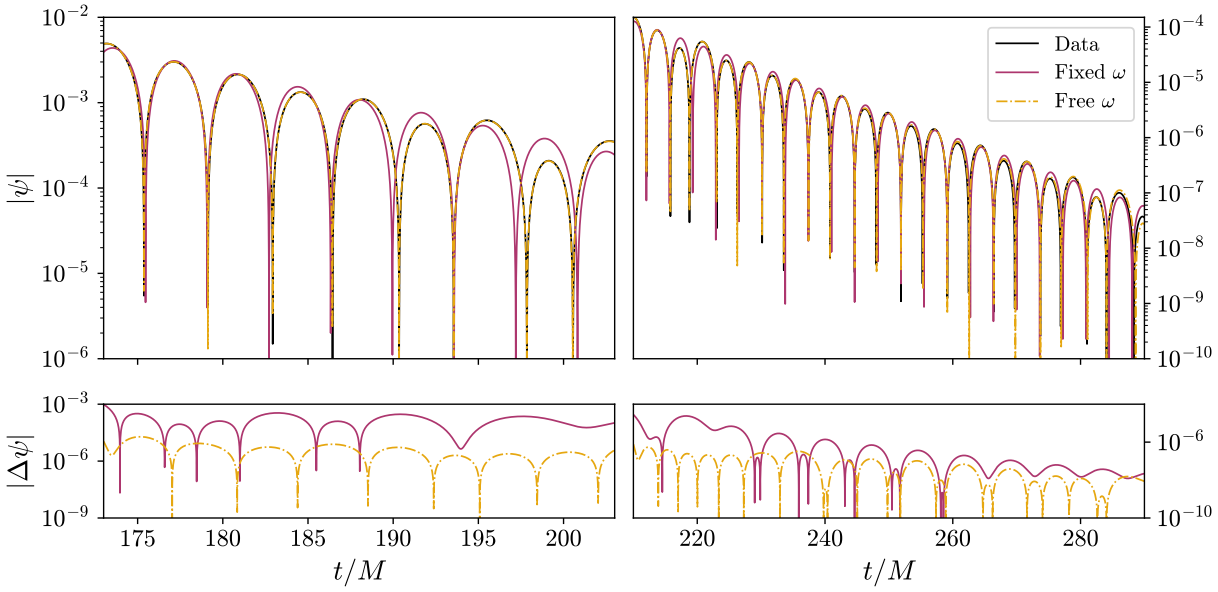

Figure C.2: Fits including 3 modes (fundamental mode and two overtones) for the signal shown in the right panel of Figure 5.4 for each of the fitting windows. We show the fit obtained with fixed frequencies (pink) and the one obtained for free frequencies (orange). The lower panel shows the difference between the fits and the data.

BIBLIOGRAPHY

[1] I. Newton, *Philosophiae Naturalis Principia Mathematica* (1687), 10.3931/e-rara-440.

[2] A. Einstein, *Zur Allgemeinen Relativitätstheorie*, *Sitzungsber. Preuss. Akad. Wiss. Berlin (Math. Phys.)* **1915** (1915) 778.

[3] J.A. Wheeler and K. Ford, *Geons, Black Holes, and Quantum Foam: A Life in Physics* (1998).

[4] W. Israel, *Event Horizons in Static Vacuum Space-Times*, *Phys. Rev.* **164** (1967) 1776.

[5] W. Israel, *Event Horizons in Static Electrovac Space-Times*, *Commun. Math. Phys.* **8** (1968) 245.

[6] B. Carter, *Axisymmetric Black Hole Has Only Two Degrees of Freedom*, *Phys. Rev. Lett.* **26** (1971) 331.

[7] S.W. Hawking, *Black Holes in General Relativity*, *Commun. Math. Phys.* **25** (1972) 152.

[8] D.C. Robinson, *Uniqueness of the Kerr Black Hole*, *Phys. Rev. Lett.* **34** (1975) 905.

[9] P.O. Mazur, *Proof of Uniqueness of the Kerr-Newman Black Hole Solution*, *J. Phys. A* **15** (1982) 3173.

[10] E.T. Newman, E. Couch, K. Chinnapared, A. Exton, A. Prakash and R. Torrence, *Metric of a Rotating, Charged Mass*, *J. Math. Phys.* **6** (1965) 918.

[11] K. Schwarzschild, *On the Gravitational Field of a Mass Point According to Einstein's Theory*, *Sitzungsber. Preuss. Akad. Wiss. Berlin (Math. Phys.)* **1916** (1916) 189 [physics/9905030].

[12] R.P. Kerr, *Gravitational Field of a Spinning Mass as an Example of Algebraically Special Metrics*, *Phys. Rev. Lett.* **11** (1963) 237.

[13] H. Reissner, *Über die eigengravitation des elektrischen feldes nach der einsteinschen theorie*, *Annalen Phys.* **355** (1916) 106.

[14] G. Nordström, *On the Energy of the Gravitational Field in Einstein's Theory*, *Koninklijke Nederlandse Akademie van Wetenschappen Proceedings Series B Physical Sciences* **20** (1918) 1238.

[15] A. Einstein, *Näherungsweise Integration der Feldgleichungen der Gravitation*, *Sitzungsberichte der Königlich Preussischen Akademie der Wissenschaften* (1916) 688.

[16] A. Einstein, *Über Gravitationswellen*, *Sitzungsber. Preuss. Akad. Wiss. Berlin (Math. Phys.)* **1918** (1918) 154.

[17] LIGO Scientific, Virgo collaboration, *GW170817: Observation of Gravitational Waves from a Binary Neutron Star Inspiral*, *Phys. Rev. Lett.* **119** (2017) 161101 [1710.05832].

[18] LIGO Scientific, Virgo collaboration, *Observation of Gravitational Waves from a Binary Black Hole Merger*, *Phys. Rev. Lett.* **116** (2016) 061102 [1602.03837].

[19] E. Mueller, *Gravitational radiation from core collapse supernovae*, *Class. Quant. Grav.* **14** (1997) 1455.

[20] L. Bildsten, *Gravitational radiation and rotation of accreting neutron stars*, *Astrophys. J. Lett.* **501** (1998) L89 [astro-ph/9804325].

[21] A. Kosowsky, M.S. Turner and R. Watkins, *Gravitational Waves from First Order Cosmological Phase Transitions*, *Phys. Rev. Lett.* **69** (1992) 2026.

[22] LIGO Scientific, Virgo collaboration, *GW150914: First Results from the Search for Binary Black Hole Coalescence with Advanced LIGO*, *Phys. Rev. D* **93** (2016) 122003 [1602.03839].

[23] LIGO Scientific, Virgo, Fermi-GBM, INTEGRAL collaboration, *Gravitational Waves and Gamma-Rays from a Binary Neutron Star Merger: GW170817 and GRB 170817A*, *Astrophys. J. Lett.* **848** (2017) L13 [1710.05834].

[24] LIGO Scientific, Virgo, KAGRA collaboration, *GW231123: A Binary Black Hole Merger with Total Mass 190–265 $M_\odot$*, *Astrophys. J. Lett.* **993** (2025) L25 [2507.08219].

[25] LIGO Scientific, Virgo, KAGRA collaboration, *GW250114: Testing Hawking's Area Law and the Kerr Nature of Black Holes*, *Phys. Rev. Lett.* **135** (2025) 111403 [2509.08054].

[26] LIGO Scientific, Virgo, KAGRA collaboration, *GWTC-4.0: Tests of General Relativity. I. Overview and General Tests*, 2603.19019.

[27] LIGO Scientific, Virgo, KAGRA collaboration, *GWTC-4.0: Tests of General Relativity. II. Parameterized Tests*, 2603.19020.

[28] LIGO Scientific, Virgo, KAGRA collaboration, *GWTC-4.0: Tests of General Relativity. III. Tests of the Remnants*, 2603.19021.

[29] LISA collaboration, *LISA Definition Study Report*, 2402.07571.

[30] ET Science Team, *Einstein Gravitational Wave Telescope Conceptual Design Study* (2011), 10.5281/zenodo.3911260.

[31] D. Reitze et al., *Cosmic Explorer: The U.S. Contribution to Gravitational-Wave Astronomy beyond LIGO*, *Bull. Am. Astron. Soc.* **51** (2019) 035 [1907.04833].

[32] E. Berti, V. Cardoso and A.O. Starinets, *Quasinormal Modes of Black Holes and Black Branes*, *Class. Quant. Grav.* **26** (2009) 163001 [0905.2975].

[33] E. Berti et al., *Black Hole Spectroscopy: From Theory to Experiment*, 2505.23895.

[34] LIGO Scientific, Virgo, KAGRA collaboration, *Black Hole Spectroscopy and Tests of General Relativity with GW250114*, *Phys. Rev. Lett.* **136** (2026) 041403 [2509.08099].

[35] ET collaboration, *The Science of the Einstein Telescope*, *JCAP* **03** (2026) 081 [2503.12263].

[36] I. Gupta, C. Afle, K.G. Arun, A. Bandopadhyay, M. Baryakhtar, S. Biscoveanu et al., *Characterizing Gravitational Wave Detector Networks: From $A^\sharp$ to Cosmic Explorer*, 2307.10421.

[37] E. Barausse et al., *Prospects for Fundamental Physics with LISA*, *Gen. Rel. Grav.* **52** (2020) 81 [2001.09793].

[38] C.M. Will, *Testing Scalar-Tensor Gravity with Gravitational Wave Observations of Inspiraling Compact Binaries*, *Phys. Rev. D* **50** (1994) 6058 [gr-qc/9406022].

[39] E. Berti et al., *Testing General Relativity with Present and Future Astrophysical Observations*, *Class. Quant. Grav.* **32** (2015) 243001 [1501.07274].

[40] S. Chandrasekhar and S.L. Detweiler, *The Quasi-Normal Modes of the Schwarzschild Black Hole*, *Proc. Roy. Soc. Lond. A* **344** (1975) 441.

[41] N. Andersson, *Evolving Test Fields in a Black-Hole Geometry*, *Phys. Rev. D* **55** (1997) 468.

[42] E.W. Leaver, *An Analytic Representation for the Quasi-Normal Modes of Kerr Black Holes*, *Proc. Roy. Soc. Lond. A* **402** (1985) 285.

[43] E.W. Leaver, *Spectral Decomposition of the Perturbation Response of the Schwarzschild Geometry*, *Phys. Rev. D* **34** (1986) 384.

[44] Y. Sun and R.H. Price, *Excitation of Quasinormal Ringing of a Schwarzschild Black Hole*, *Phys. Rev. D* **38** (1988) 1040.

[45] E. Berti and V. Cardoso, *Quasinormal Ringing of Kerr Black Holes. I. The Excitation Factors*, *Phys. Rev. D* **74** (2006) 104020 [gr-qc/0605118].

[46] S. Bernuzzi, A. Nagar and R. De Pietri, *Dynamical Excitation of Space-Time Modes of Compact Objects*, *Phys. Rev. D* **77** (2008) 044042 [0801.2090].

[47] M. Giesler, M. Isi, M.A. Scheel and S.A. Teukolsky, *Black Hole Ringdown: The Importance of Overtones*, *Phys. Rev. X* **9** (2019) 041060.

[48] V. Baibhav, M.H.-Y. Cheung, E. Berti, V. Cardoso, G. Carullo, R. Cotesta et al., *Agnostic Black Hole Spectroscopy: Quasinormal Mode Content of Numerical Relativity Waveforms and Limits of Validity of Linear Perturbation Theory*, *Phys. Rev. D* **108** (2023) 104020.

[49] M. De Amicis, E. Cannizzaro, G. Carullo and L. Sberna, *Dynamical Quasinormal Mode Excitation*, *Phys. Rev. D* **113** (2026) 024048 [2506.21668].

[50] F. Crescimbeni, X.J. Forteza and P. Pani, *Testing Gravity with Black Hole Ringdown Amplitudes*, *Phys. Rev. D* **113** (2026) 044064 [2510.11782].

[51] T. Regge and J.A. Wheeler, *Stability of a Schwarzschild Singularity*, *Phys. Rev.* **108** (1957) 1063.

[52] F.J. Zerilli, *Effective Potential for Even-Parity Regge-Wheeler Gravitational Perturbation Equations*, *Phys. Rev. Lett.* **24** (1970) 737.

[53] C.V. Vishveshwara, *Scattering of Gravitational Radiation by a Schwarzschild Black Hole*, *Nature* **227** (1970) 936.

[54] S.A. Teukolsky, *Perturbations of a Rotating Black Hole. I. Fundamental Equations for Gravitational, Electromagnetic, and Neutrino-Field Perturbations*, *Astrophys. J.* **185** (1973) 635.

[55] S. Chandrasekhar, *The Mathematical Theory of Black Holes*, Oxford University Press (1985).

[56] V. Cardoso, S. Biswas and S. Sarkar, *The Physics of Black Holes and Their Environments: Consequences for Gravitational Wave Science*, 11, 2025 [2511.14841].

[57] J. Mathews, *Gravitational Multipole Radiation*, *J. Soc. Indust. Appl. Math.* **10** (1962) 768.

[58] F.J. Zerilli, *Gravitational Field of a Particle Falling in a Schwarzschild Geometry Analyzed in Tensor Harmonics*, *Phys. Rev. D* **2** (1970) 2141.

[59] M. Maggiore, *Gravitational Waves. Vol. 2: Astrophysics and Cosmology*, Oxford University Press (2018).

[60] V. Ferrari, L. Gualtieri and P. Pani, *General Relativity and Its Applications: Black Holes, Compact Stars and Gravitational Waves*, CRC Press (2020).

[61] R.M. Wald, *General Relativity*, Chicago University Press (1984), 10.7208/chicago/9780226870373.001.0001.

[62] G. Wentzel, *Eine Verallgemeinerung der Quantenbedingungen für die Zwecke der Wellenmechanik*, *Z. Phys.* **38** (1926) 518.

[63] H.A. Kramers, *Wellenmechanik und halbzahlige Quantisierung*, *Z. Phys.* **39** (1926) 828.

[64] L. Brillouin, *La mécanique ondulatoire de Schrödinger; une méthode générale de résolution par approximations successives*, *J. Phys. Radium* **7** (1926) 353.

[65] B.F. Schutz and C.M. Will, *Black Hole Normal Modes - A Semianalytic Approach*, *Astrophys. J. Lett.* **291** (1985) L33.

[66] S. Iyer and C.M. Will, *Black Hole Normal Modes: A WKB Approach. I. Foundations and Application of a Higher Order WKB Analysis of Potential Barrier Scattering*, *Phys. Rev. D* **35** (1987) 3621.

[67] V. Cardoso, A.S. Miranda, E. Berti, H. Witek and V.T. Zanchin, *Geodesic Stability, Lyapunov Exponents and Quasinormal Modes*, *Phys. Rev. D* **79** (2009) 064016 [0812.1806].

[68] W.H. Press, *Long Wave Trains of Gravitational Waves from a Vibrating Black Hole*, *Astrophys. J. Lett.* **170** (1971) L105.

[69] G. Calabrese, L. Lehner, O. Reula, O. Sarbach and M. Tiglio, *Summation by Parts and Dissipation for Domains with Excised Regions*, *Class. Quant. Grav.* **21** (2004) 5735.

[70] B. Gustaffson, H. Kreiss and J. Oliger, *Time Dependent Problems and Difference Methods*, Wiley, New York (1995).

[71] H. Witek, V. Cardoso, C. Herdeiro, A. Nerozzi, U. Sperhake and M. Zilhão, *Black Holes in a Box: Toward the Numerical Evolution of Black Holes in AdS Space-Times*, *Phys. Rev. D* **82** (2010) 104037.

[72] The Center of Gravity, "Data and Routines."

[73] Y. Hua and T.K. Sarkar, *Generalized Pencil-of-Function Method for Extracting Poles of an EM System from Its Transient Response*, *IEEE Trans. Antennas Propag.* **37** (1989) 229.

[74] M. De Amicis and E. Cannizzaro, *Post-Minkowskian Expansion of the Prompt Response in a Schwarzschild Background*, 2601.11706.

[75] N. Andersson, *Excitation of Schwarzschild Black Hole Quasinormal Modes*, *Phys. Rev. D* **51** (1995) 353.

[76] R.H. Price, *Nonspherical Perturbations of Relativistic Gravitational Collapse. I. Scalar and Gravitational Perturbations*, *Phys. Rev. D* **5** (1972) 2419.

[77] E.S.C. Ching, P.T. Leung, W.M. Suen and K. Young, *Late-Time Tail of Wave Propagation on Curved Space-Time*, *Phys. Rev. Lett.* **74** (1995) 2414 [gr-qc/9410044].

[78] E.S.C. Ching, P.T. Leung, W.M. Suen and K. Young, *Wave Propagation in Gravitational Systems: Late-Time Behavior*, *Phys. Rev. D* **52** (1995) 2118.

[79] T. Bochud and D. Challet, *Optimal Approximations of Power-Laws with Exponentials*, physics/0605149.

[80] S.R. Dolan and A.C. Ottewill, *On an Expansion Method for Black Hole Quasinormal Modes and Regge Poles*, *Class. Quant. Grav.* **26** (2009) 225003 [0908.0329].

[81] J. Redondo-Yuste, V. Cardoso, C.F.B. Macedo and M. van de Meent, *Eternal Binaries*, *Phys. Rev. D* **107** (2023) 124025 [2304.02039].

[82] V. Cardoso, G. Carullo, M. De Amicis, F. Duque, T. Katagiri, D. Pereniguez et al., *Hushing Black Holes: Tails in Dynamical Spacetimes*, *Phys. Rev. D* **109** (2024) L121502 [2405.12290].

[83] Y. Hua and T.K. Sarkar, *Matrix Pencil Method for Estimating Parameters of Exponentially Damped/Undamped Sinusoids in Noise*, *IEEE Trans. Acoust. Speech Signal Process.* **38** (1990) 814.

[84] E. Berti, V. Cardoso, J.A. Gonzalez and U. Sperhake, *Mining Information from Binary Black Hole Mergers: A Comparison of Estimation Methods for Complex Exponentials in Noise*, *Phys. Rev. D* **75** (2007) 124017 [gr-qc/0701086].

[85] G.H. Golub and C.F. Van Loan, *Matrix Computations*, Johns Hopkins Studies in the Mathematical Sciences, 4 ed. (2013).

[86] Z.-H. Yang, L.-B. Wu, X.-M. Kuang and W.-L. Qian, *QNM Families: Classification and Competition*, 2510.02033.